Studying the impact of electron bunch characteristics on plasma wakefield performance using particle-in-cell simulations

Nico Wrobel

Geboren am: 10. März 2001 in Hoyerswerda

Bachelor-Arbeit

zur Erlangung des akademischen Grades

Bachelor of Science (B. Sc.)

Gutachter

Prof. Dr. Ulrich Schramm
Prof. Dr. Thomas E. Cowan

Betreuer

Dr. Richard Pausch

Eingereicht am: 6. Januar 2023

Abstract

The accessibility of plasma-based accelerators was greatly expanded by the realization of laser wakefield accelerator (LWFA)-driven plasma wakefield accelerators (PFWA). This development speeds up research on PWFA significantly. In this thesis, 3D particle-in-cell-simulations were used to analyze driver parameters for a PWFA to achieve maximal energy gain for a hypothetical witness beam. Only small increases in witness energy were found when drivers with high kinetic energy were compared. In contrast, great witness energy increases result when the divergence of the driver gets reduced. The transformation of a driver in plasma is analyzed, and the influence of the wakefield on it is discussed. Additionally, evidence for non-constant peak energy is presented, with energy losses in the MeV scale independent from driver characteristics. This could require adjustments to the charge reconstruction of the LWFA-bunch after the PWFA stage.

Kurzfassung

Die Verfügbarkeit von Plasma-basierten Beschleunigern wurde durch die Verwirklichung von Laser-Wakefield-Beschleuniger (LWFA) getriebenen Plasma-Wakefield Beschleunigern (PWFA) stark vereinfacht. Diese Entwicklung erlaubt eine breitere Erforschung von PWFA. 3D Particle-in-Cell Simulationen wurden in dieser Arbeit verwendet, um die Treiberparameter von PWFA zu analysieren, damit ein maximaler Energiegewinn für einen hypothetischen Witness erreicht werden kann. Nur kleine Erhöhungen der Witness Energie konnten festgestellt werden, wenn die kinetische Energie des Treibers erhöht wurde. Im Gegensatz dazu konnten hohe Energiegewinne durch das Senken der Divergenz des Treibers erreicht werden. Die Transformation des Treibers im Plasma wurde analysiert und der Einfluss des Wakefields auf diesen diskutiert. Zusätzlich werden Indizien für eine nicht konstante Peak-Energie vorgestellt, mit Energieverlusten im MeV-Bereich, unabhängig von den initialen Parametern des Treibers. Dies könnte eine leichte Anpassung der Ladungsrekonstruktion des LWFA-Bunch nach der PWFA-Phase erforderlich machen.

Table of Contents

1. Introduction

The combination of laser wakefield acceleration (LWFA) and plasma wakefield acceleration (PWFA) could be a critical step in boosting research with plasma wakefield accelerators. Their compactness allows for small facilities to still operate their own PWFA while the LWFA's high repetition rate allows for an significant time reduction when performing statistical analysis.

Since the invention of the first particle accelerators in the late 19th century [1], the development of new radio frequency (RF) accelerators progressed at a fast pace due to their practicality in applied science, cancer therapy, and basic research, like particle physics. In the latter example, considerable advancements in our understanding of the universe could be made thanks to RF accelerators, with modern particle physics and the standard model being funded on the discoveries made with them.

Still, modern RF accelerators are restricted by the sustainability of the metal cavities enclosing them, allowing only acceleration fields up to around $100\,\mathrm{MV\,m^{-1}}$. This limits applications and research in small-scale laboratories, as huge-scale accelerators are needed to achieve the energies used in modern particle physics. For the discovery of the Higgs boson at the Large Hadron Collider, a center-of-mass energy of $8\,\mathrm{TeV}$ [2] was needed for the proton-proton collisions. A synchrotron with a $27\,\mathrm{km}$ long acceleration distance was required for this achievement.

In 1979, Tajima and Dawson proposed a new type of particle accelerator [3]. The so-called laser wakefield acceleration uses a high-intensity laser pulse as a driver, which excites a wakefield when sent through a plasma. They theorized that charged particles could be accelerated by the strong electric fields in the cavities of this wakefield. Later, in 1985, a similar acceleration scheme, the plasma wakefield acceleration, was theorized by Chen and Dawson [4], where charged particles were used as drivers to excite the wakefield with similar strong electric fields. Both proposals were later verified in experiment.

Even though both acceleration techniques are similar in concept, for the longest time, research on them was done primarily independently from each other. Only in recent years, proposals [5] were made for the so-called LWFA-driven PWFA (LPWFA), which uses the charged particle bunch generated by a LWFA stage as the driver for a PWFA stage. First experimental demonstrations of this concept [6] could achieve high acceleration gradients up to $100\,\mathrm{GV\,m^{-1}}$, showing the high potential of such small-scale accelerators. This would allow for even faster experimental research to answer open questions and enable practical applications.

A considerable part of the fast advent of LWFA and PWFA can be attributed to the particle-in-cell (PIC)-model and its software implementation in PIC-codes. This model is used to discretize the physical environment and break down complex electromagnetic interactions between

particles into a set of steps that a computer can process. Its application as a simulation of the dynamics of plasma and electromagnetic waves or charged particles was found helpful in different fields of physics, for example in the astrophysics of solar plasmas.

When first proposing LWFA, PIC-codes were already used by Tajima and Dawson to show the potential of their concept before first experiments could be conducted. With the fast development of high-performance computing and more efficient software, PIC-codes today can simulate three-dimensional, relativistic plasma interactions in short time spans and are used to find the optimal driver and plasma parameters to be tested in experiments.

This thesis discusses the characteristics of the electron bunch used to excite the wakefield in the PWFA. Using electron bunches from a preliminary LWFA stage opens new possibilities for experimental research on such drivers. Therefore, there is great interest in the initial properties of the bunch, as it shapes the form and efficiency of the wakefield. This work puts focus on the interaction between plasma and driver, especially on the changes to the shape of the driver and the resulting energy gain from potentially accelerated particles.

These studies are done in PIConGPU, a relativistic PIC-code developed at the Helmholtz-Zentrum Dresden-Rossendorf (HZDR). PIC-simulations allow for precise formulation of the characteristics of the bunch. The results are compared for different initial conditions of the driver to propose possible directions the experimental research could take when optimizing bunch parameters.

Lastly, research was done on the so-called peak energy, an important measurement of bunch characteristics between the two stages of the LPWFA [7]. Limits to the constancy of this quantity are investigated, as this is an essential experimental assumption that needed verification via simulation.

In chapter 2, the theoretical background is established for both the physics of PWFA and the usage of PIC-code. Particular focus is put on the implementation in PIConGPU. Then the setup of the used simulations is discussed in chapter 3. At last, the discussion of the research results follow in chapter 4. The chapter is split into two parts. First, the analysis of the driver parameters and the resulting impact on driver transformation and wakefield are presented in section 4.1. Afterward, a closer look at changes in the peak energy was taken in section 4.2, followed by the final conclusion in chapter 5.

2. Theoretical background

2.1. Plasma Wakefield acceleration

PWFA is a novel particle accelerator concept [4] with the possibility to produce high accelerating electric fields (more than $100\,$GV/m). This allows for higher energy gains per meter and thus several order of magnitude smaller accelerators, compared to conventional RF accelerators.

PWFA works by sending a bunch of charged particles (also called drive beam or driver) with relativistic speed ($v_{\mathrm{beam}} \approx c$) into a neutral plasma. Multiple sources are possible for this beam and will be further discussed in subsection 2.1.1. In this thesis, the beam consists of electrons but research on other species like protons or positrons [8] is made as well. To be easily ionized, the plasma is often formed by light weight gases like lithium (or even hydrogen or helium in newer experiments [7]), ionized either by the drive beam itself or a dedicated ionization laser or discharge.

When entering the plasma, the drive beam interacts with the plasma electrons, while the effect on the ions can be neglected at the time scale of the electron response. The electric field of the bunch pushes the electrons out of its way, comparable to a snowplow. This leaves an electron free cavity behind, starting from the center of the driver while the expelled electrons culminate at the borders of the cavity. As the ions are not moving, this cavity is positively charged, meaning it acts as an attractive force to the plasma electrons. When being pulled back towards the center of the cavity, the electrons overshoot and produce another cavity. The result is electron oscillation, where multiple cavities form behind the beam as seen in Figure 2.1.

This train of cavities is called the wakefield. If the electron density in these cavities is several orders of magnitude smaller than in the rest of the plasma, this state is called the blowout regime, else it is called the linear regime. When injecting a charged particle bunch, called the witness beam, into the wakefield, it sees fields acting from different directions due to the gradient towards the center of the positive cavity.

For a witness beam in propagation direction, consisting of negative charged particles, the electric field accelerates towards the center of the cavity while decelerating when reaching its front half. Perpendicular to the direction of propagation are electric fields pointing towards the center and magnetic fields rotating around the propagation axis, resulting in focusing of the witness beam. In contrast there are defocusing forces between the cavities, as the oscillating electrons are densest here. When witness electrons are injected into the back of the cavity, they will be accelerated while the cavity itself moves at near light speed with the driver. These accelerating forces peak when the wakefield is in the blowout regime, therefore achieving
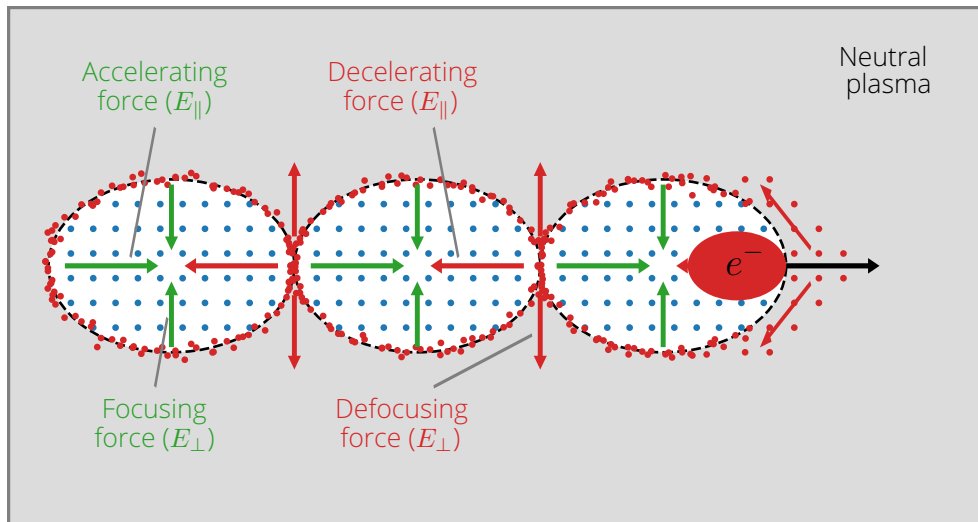
Figure 2.1.: The blowout regime of a PWFA stage with an electron driver at the front. Alternating accelerating/decelerating fields in longitudinal and focusing/defocusing fields in transverse direction form in the cavities. Blue dots mark the remaining ions, red dots the electrons. Figure similar to [9].

blowout as long as possible is a goal of PWFA.

Near light speed, the velocity of the witness beam will not increase in a meaningful way. The witness electrons would therefore be trapped in the accelerating part of the cavity, resulting in a net increase of their momentum and energy.

2.1.1. LWFA driven PWFA

For a long time, a big downside of PWFA was the creation of the relativistic drive beams, as this would need kilometer long RF accelerators as a preliminary stage. Recent research [6] investigated the potential of the so called LPWFA. Here, the witness bunch of an LWFA was used as driver for the PWFA, allowing for a very compact design.

LWFA is very similar to PWFA. Instead of charged particles, a laser is shot into a plasma to drive the wakefields, also generating hundreds of GV/m of accelerating fields. The witness bunch can be accelerated to higher speeds than the speed of the laser in the plasma, resulting in dephasing, where the witness beam is fast enough to reach the center of the cavity and get decelerated. This limits the acceleration capabilities of the LWFA. Still, the resulting witness bunch can be used as the driver for a PWFA.

Experimental setups for LPWFA (see Figure 2.2) consist of a laser initiating a LWFA stage in a gas jet. Both, the accelerated witness bunch and the laser are leaving the jet into vacuum, where a metal foil is installed to block the laser and let only the particle beam through. Thus, only the witness bunch makes it to the next gas jet, serving as the driver for the PWFA stage and accelerating injected electrons. This hybrid scheme has the potential to advance the PWFA research further and make it more accessible to small scale labs [6].

Peak energy
The energy with the highest charge density of driver or witness particles is called peak energy. In experiment, it is an important measurement as it provides the beam charge of a witness beam leaving a LWFA stage [7]. The peak energy of the driver is assumed to stay constant
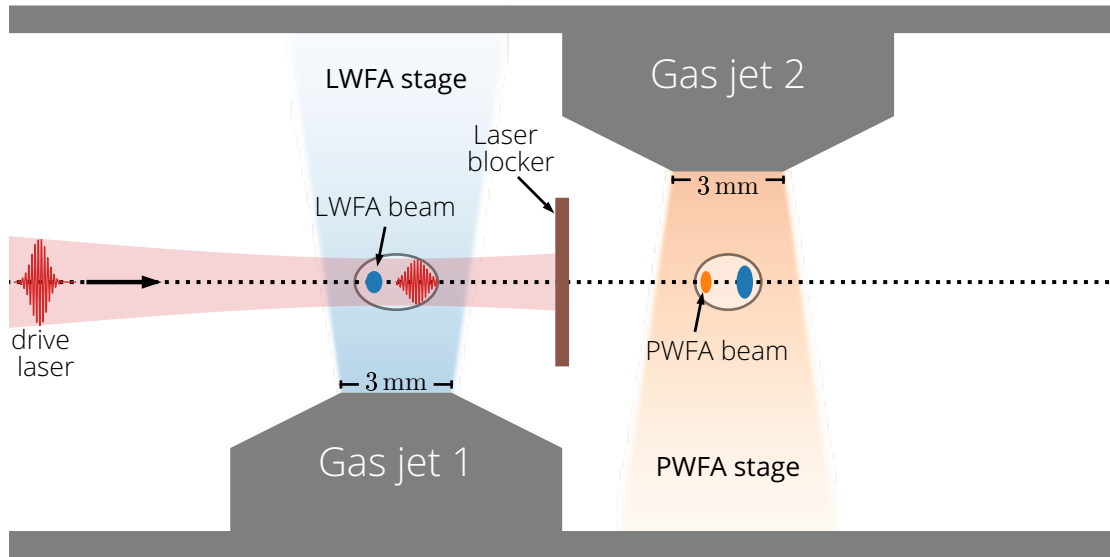
Figure 2.2.: Example for an LPWFA setup. The laser starts an LWFA in the first gas jet. The resulting LWFA beam is then used to start a PWFA in a second gas jet. A metal foil blocks the laser after the first stage. Figure similar to [5]

during a PWFA stage, therefore information about the driver before entering the PWFA can be obtained in a LPWFA.

Section 4.2 will discuss evidence, that the peak energy is reduced during the PWFA stage, and the assumption of constant peak energy therefore might be an acceptable assumption with current experimental uncertainties but needs to be considered for future experiments .

2.2. PIConGPU

To simulate complex driver-plasma interactions efficiently, the particle-in-cell (PIC)-method is often chosen. There are many different code implementations developed to overcome prevailing technical limitations. For this thesis PIConGPU [10, 11] is used, a relativistic PIC-code, which specializes in parallelization of the computational steps. Therefore it is designed to work on GPUs instead of CPUs. We will start with an introduction to the PIC method in general in subsection 2.2.1. In the following subsection, we discuss further how certain inputs and outputs are handled in PIConGPU.

2.2.1. Particle-in-cell model

PIC-code models particles in a simulation box and is a common approach to numerically solve the Vlasov-Maxwell system of equations by applying various simplifications. This system described the particles as a distribution function $f_s(\vec{x}, \vec{p}, t)$ of time t, position $\vec{x}$ and momentum $\vec{p}$ for every particle species s [11, 12]. This distribution must now satisfy the collisionless Boltzmann equation, also called Vlasov equation[13], see Equation 2.1.

$$\frac{\mathrm{d}f_s}{\mathrm{d}t} = \frac{\partial f_s}{\partial t} + \frac{\partial \vec{x}}{\partial t}\frac{\partial f_s}{\partial \vec{x}} + \frac{\partial \vec{p}}{\partial t}\frac{\partial f_s}{\partial \vec{p}} = 0 \qquad (2.1)$$

Using the Nabla-Operator and the derivatives of $\vec{x}$ and $\vec{p}$, we get Equation 2.2 with the Lorentz factor γ, the species mass m_s and the Lorentz Force $\vec{F}_L$, see Equation 2.3.
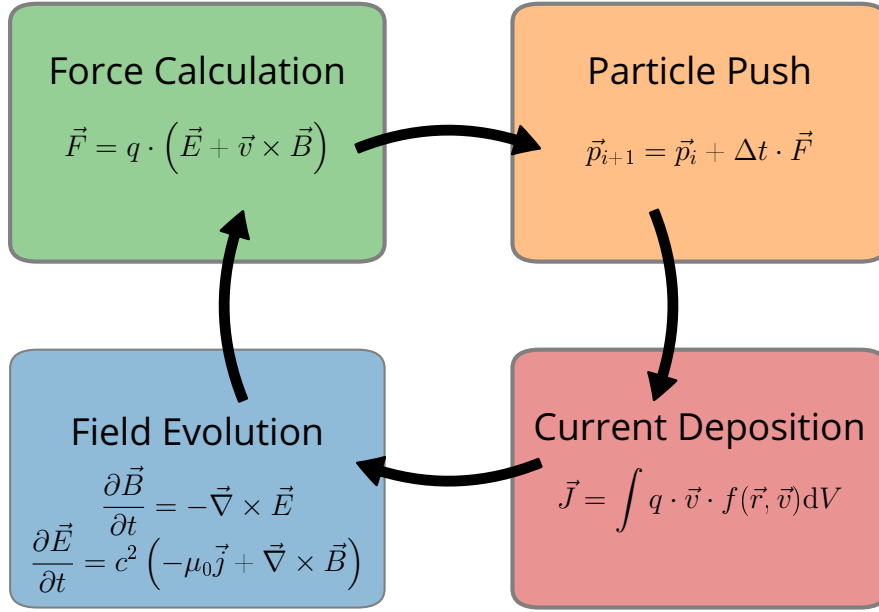
Figure 2.3.: The PIC-cycle. In PIConGPU, every timestep starts with the force calculation. Figure taken from [15]

$$\partial_t f_s + \frac{\vec{p}}{m_s \gamma} \vec{\nabla}_{\vec{x}} f_s + \vec{F}_L \vec{\nabla}_{\vec{p}} f_s = 0 \tag{2.2}$$

$$\vec{F}_L = q_s \left(\vec{E} + \vec{v} \times \vec{B} \right) \tag{2.3}$$

To be a self-consistent set of electro-magnetic equations, the Maxwell equations (see Equation 2.4) need to be fulfilled by our $\vec{E}$- and $\vec{B}$-fields. Here ρ_s and $\vec{J}_s$ are the charge and current density for a given species s.

$$\vec{\nabla} \cdot \vec{E} = \frac{1}{\epsilon_0} \sum_s \rho_s$$

$$\vec{\nabla} \cdot \vec{B} = 0$$

$$\vec{\nabla} \times \vec{E} = -\frac{\partial \vec{B}}{\partial t} \tag{2.4}$$

$$\vec{\nabla} \times \vec{B} = \mu_0 \left(\sum_s \vec{J}_s + \epsilon_0 \frac{\partial \vec{E}}{\partial t} \right)$$

The PIC method now makes several simplifications, so these requirements can be implemented. At first, the time needs to be discretized into timesteps with length Δt after which our distribution is updated. The system of equations above must then be broken down into a system of computations, which will be processed every timestep. This system is called the PIC-cycle [14], which can be seen in Figure 2.3.

Instead of the complex high-dimensional distribution function $f_s(\vec{x}, \vec{p}, t)$, we look at a simulation box in 3 dimensions of space and describe the distribution for a species as discrete macroparticles in this box [16]. The movement of these macroparticles is then described by their position and momentum, the acceleration from the acting force depends on their set mass m, charge q and weighting w. The weighting is determined by the assignment density
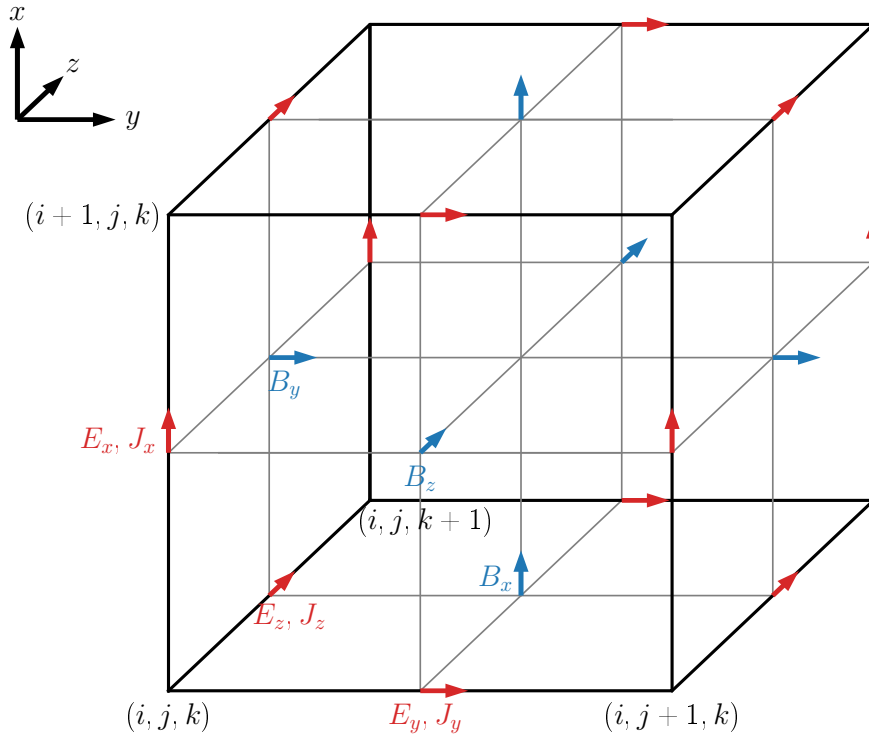
Figure 2.4.: One Yee-cell with components of the electric $\vec{E}$-field, the magnetic $\vec{B}$-field and the current density $\vec{J}$ drawn in. Note, that fields are calculated between the grid-points. Image similar to [11]

function which the macroparticle represents and can also be seen as the number of real particles for each macroparticle. In this thesis, the assignment function of the driver particles is given by a piecewise quadratic spline.

At last, the fields need to be divided into the so-called Yee-grid [17], which can be seen in Figure 2.4. The corresponding fields are placed between the grid-points, motivated by the fact that for the later described centered finite difference, the spatial derivative of the fields lies between these fields. At these points, the time derivatives are calculated, and therefore the grid-points positioned.

Force calculation

When the macroparticles and the corresponding fields at each grid-point (i, j, k) at a timestep n are given, the calculation of the next timestep can start. At first, the grid fields are interpolated to the position of the macroparticles so that the acting forces can be calculated. PIConGPU uses trilinear interpolation for this task [11, 14], a 3D extension of linear interpolation. Then the acting Lorentz Force can be calculated by Equation 2.3. With the forces at each particles position, now the particle pusher can calculate the new positions and momenta of the particle distributions.

Particle pusher

There exist multiple implementations for this problem in PIConGPU, the standard one being the relativistic Boris-pusher [18], which conserves the phase-space volume [11]. Instead of centering the $\vec{B}$-field on integer timesteps, the momentum at half integer timesteps gets calculated by only applying the first part of the Lorentz-Force $\vec{F}_L$ (the Coulomb-force) for $\Delta t/2$. Afterward, the magnetic part of the Lorentz-Force is calculated at this half timestep $n + 1/2$

and then added to the momentum, amounting for the full timestep. At last, the Coulomb force is applied again for half a timestep, so the momentum at the full step $n + 1$ is returned [15, 19]. Updating the particle position is done by applying the Euler-method, see Equation 2.5.

$$\vec{x}^{(n+1)} = \vec{x}^{(n)} + \Delta t \frac{\vec{p}^{(n+1)}}{\gamma m} \tag{2.5}$$

Current deposition

For the next step of the PIC-cycle, the current density $\vec{J}$ is calculated with Esirkepov's current deposition method [20]. The change in current density between two grid-points is calculated by accumulating nearby macroparticles with respect to their velocity, charge, assignment functions and change in position between two time steps. As for the components of the $\vec{E}$-field, the current density components are stored not on but between the grid points, as seen in Figure 2.4.

Field evolution

At last, the new fields are calculated at each grid-point. The first two Maxwell equations Equation 2.4 are assumed to be fulfilled at initialization, in general with $\rho = 0$. This means, our box is charge neutral at the start, resulting in mirror charges when we don't have a completely neutral setup. For the rest of the simulation, only the last two of Maxwell's equation need to be solved, which is done by numerical integration. Multiple field solver implementations can be used in PIConGPU. In this thesis the Finite-Difference Time-Domain method is used in the form of the ArbitraryOrderFDTD solver [11]. It uses centered finite differences with a given number M of neighbor grid-points around our wanted point. Here, the time derivative is always replaced by a second order approximation, shown for a general function $u(i\Delta x, j\Delta y, k\Delta z, n\Delta t)$ in Equation 2.6. The spatial derivative for u of order $2M$ can be calculated by Equation 2.7 [11] with g_l^{2M} as a weighting factor (see Equation 2.8).

$$\partial_t u(i\Delta x, j\Delta y, k\Delta z, n\Delta t) = \frac{u_{i,j,k}^{n+1/2} - u_{i,j,k}^{n-1/2}}{\Delta t} \tag{2.6}$$

$$\partial_x u(i\Delta x, j\Delta y, k\Delta z, n\Delta t) = \sum_{l=1/2}^{M-1/2} \left[g_l^{2M} \frac{u_{i+l,j,k}^{n} - u_{i-l,j,k}^{n}}{\Delta x} \right] \tag{2.7}$$

$$g_l^{2M} = \frac{(-1)^{l-1/2}}{2l^2} \frac{((2M-1)!!)^2}{(2M-1-2l)!!(2M-1+2l)!!} \tag{2.8}$$

We use $M = 4$ neighboring grid-points, resulting in an eight-order approximation. The resulting weighting factors in Table 2.1 give us the full numerical form of the 2 Maxwell equations, which can be found in the appendix in Appendix A.

$g_{1/2}^{2\cdot4}$	$11\,962.891 \times 10^{-4}$
$g_{3/2}^{2\cdot4}$	-797.526×10^{-4}
$g_{5/2}^{2\cdot4}$	95.703×10^{-4}
$g_{7/2}^{2\cdot4}$	-6.976×10^{-4}

Table 2.1.: Weighting factors for 8th order spacial derivatives.

With the numerical derivatives, we first calculate $\vec{E}^{(n+1)}$, then $\vec{B}^{(n+3/2)}$, giving us our fields at each grid-point. Afterwards the PIC-cycle can repeat.

2.2.2. Dispersion relation

Discretization of the phase space yields us different dispersion relations than for real electromagnetic waves. For the used Arbitrary Order Finite Differences, this relation between frequency ω and wave vector components k_x, k_y and k_z are found in Equation 2.9 and Equation 2.10 [11].

$$\omega = \frac{2}{\Delta t} \arcsin \xi \tag{2.9}$$

$$\xi = \left[\sum_{l=1/2}^{M-1/2} g_l^{2M} \frac{\sin(k_x l \Delta x)}{\Delta x} \right]^2 + \left[\sum_{l=1/2}^{M-1/2} g_l^{2M} \frac{\sin(k_y l \Delta y)}{\Delta y} \right]^2 + \left[\sum_{l=1/2}^{M-1/2} g_l^{2M} \frac{\sin(k_z l \Delta z)}{\Delta z} \right]^2 \tag{2.10}$$

Δt is here the time discretization, Δx, Δy and Δz are the grid spacings and g_l^{2M} is the weighting factor, given in Equation 2.8.

ξ is maximal when the squares of the sine functions return 1. Additionally, the arcsine in Equation 2.9 sets the condition $\xi_{max} < 1$. Together these result in a stability condition between the spacing of the time steps and the grid, see Equation 2.11.

$$c\Delta t < \frac{1}{\left[\sum_{l=1/2}^{M-1/2} (-1)^{l-\frac{1}{2}} g_l^{2M} \right] \sqrt{\frac{1}{\Delta x^2} + \frac{1}{\Delta y^2} + \frac{1}{\Delta z^2}}} \tag{2.11}$$

Generally, ξ_{max} is chosen as 0.995, which is low enough to fulfill Equation 2.11. It should not be chosen too low, as the phase velocity $v_p = \omega/k$ would be reduced as well. This could result in numerical Cherenkov radiation when the charged particles move faster than v_p, giving back unphysical results.

Increasing the terms which are taken into account for the finite difference approximation increases the accuracy of the approximation. It, therefore, results in less numerical Cherenkov radiation than low order solver, like the standard second-order Yee-solver. As an alternative approach, a Lehe-solver [21] is implemented in PIConGPU. The goal of this solver is to avoid numerical Cherenkov radiation, that is emitted for the Yee- or ArbitraryOrderFDTD solvers.

Tests of this solver showed that this implementation of the Lehe solver is not suitable for the required initialization methods of PWFA simulations, as highly nonphysical electric fields appeared during the simulations. Therefore, the ArbitraryOrderFDTD solver of eighth order is still used for this thesis.

2.2.3. Boundary conditions

The behavior of the fields and particles at the borders of the simulation box is determined by the boundary conditions. For fields there exist two options in PIConGPU: either the boundaries are periodic or absorbing. In the first case, when a field reaches the boundary, it wraps around the box and appears again at the other side on the same axis. In the latter case, the fields start to be absorbed at a set distance from the border, with the strength of the absorption increasing towards the boundary, until it fully vanishes at the border.

The perfectly matched layer (PML)-absorber is used as the standard in PIConGPU. When using periodic conditions, the condition can be toggled for each individual axis (periodic behavior in longitudinal direction is normally not wanted for PWFAs).

Particles follow the periodicity of the fields but have different option when no periodic conditions apply. For this thesis, absorbing conditions are used, so all particles crossing the border are deleted from the simulation.

2.2.4. Acceleration pusher

As will be later discussed in section 3.2, the initial bunch from the LWFA stage is modeled with given position and momentum of the macroparticles. No corresponding fields are given, thus they need to be created by the simulation. This is an iterative process where we first apply a constant force in longitudinal direction to our bunch and calculate backwards how it looked a given number of timesteps before [22]. Then we can put it in the simulation, apply the same force and let it create a corresponding field through the PIC-cycle (see subsection 2.2.1), while the bunch moves to its initial position in phase space.

Problem is, PIConGPU expects a charge free box, so when electrons are placed in the box it will automatically assume a positive mirror charge behind every particle. This mirror charge would then pull back our real bunch, slowing it down in the process. Therefore, the acceleration pusher is used instead of the Boris pusher. Here, the constant accelerating force is the only acting force, completely ignoring the created fields. The mirror charge is left behind while the bunch moves outside of its reach and the corresponding fields build up. When the bunch arrives at its initial position, the pusher can be switched to a physical pusher and the real simulation can proceed.

2.2.5. openPMD

PIConGPU supports multiple plugins which act as outputs for the simulated data. Most of the analysis in this thesis is done through the output of the openPMD-api [23] plugin. It returns the simulation data according to the openPMD standard, which provides a unified convention for names and attributes of simulated data [24].

Data will be stored for the fields and the particle species for given timesteps. Field data is stored per grid-point and includes the $\vec{E}$- and $\vec{B}$-field as well as the charge- and energy density for every particle species. For particles, the position (cell + position in cell), momentum and weighting can be read among other quantities.

Additional non-standard attributes can be defined and stored. A use case of this will be described in section 3.1. All data is stored in PIConGPU-internal units, multiplication factors are stored as well for conversion to SI units.

3. Setting up a PWFA simulation with PIConGPU

The goal of the setup is to simulate a PWFA, assuming a LWFA generated electron bunch as driver. It would be possible to let PIConGPU run both stages but creating the bunch via script makes it easier to control the wanted parameters and is faster than a full LWFA simulation. Therefore, an electron beam which emulates a witness bunch leaving a LWFA is generated with a python script (see section 3.2). Afterwards the corresponding fields and the plasma interaction are computed with PIConGPU. The parameters for the simulation will be explained in section 3.1, before we go further to the initialization of the plasma in section 3.3.

3.1. Simulation parameters

For all setups, a box consisting of $1024 \times 2048 \times 1024$ grid cells for field calculation is used. The currently simulated volume measures $90.7\,\mu m \times 181.5\,\mu m \times 90.7\,\mu m$ and moves with light speed c in the direction of propagation. In contrast to experiment, this direction of propagation is labeled as y-axis. Instead of y, the co-moving $\zeta = y - ct$ coordinate is used in chapter 4. Every calculated timestep has a duration of $1.33 \times 10^{-16}\,s$.

For the first 10 191 timesteps (corresponds to a distance of 40.5 µm), the acceleration pusher (see subsection 2.2.4) acts on the bunch with a constant force, created by an electric field with a strength of 620.4 MV/mm. Afterwards the Boris pusher is used. The boundary of the box is using a PML-absorber in all directions.

Additional to the standard openPMD data, an ID is stored for every bunch particle for back tracing, as well as field probe properties, which store the experienced electric and magnetic field for every particle. This is only used for visualization of the forces on the bunch, while grid data is used for calculation of the energy gain.

3.2. Initialization of an electron bunch from script

To save on computational power, a python script generates the electron bunch after a LWFA stage from given parameters. Parameters which can be measured in experiments are used, so a comparison is easily possible, but they need to be converted to other statistical quantities like the standard deviation. The parameter values used are based on recent experimental results [6, 7, 25].

The number of bunch particles is derived from the total charge, chosen as 400×10^{-12} C, which results in roughly 250×10^9 electrons. After leaving the LWFA stage, the position of the particles is assumed to be normally distributed in each direction. For the transversal position this distribution is centered around the axis with the standard deviation $\sigma_{x,z}$ derived from Equation 3.1 with the root mean square (rms) radius $r_{rms} = 10\,\mu$m.

$$\sigma_{x,z} = \frac{r_{rms}}{\sqrt{2}} \tag{3.1}$$

The $1/\sqrt{2}$ factor is a geometric factor, originating from the fact that for a normal distribution with zero mean, the rms and the standard deviation are identical. The rms radius can then be calculated by $r_{rms}^2 = \sigma_x^2 + \sigma_z^2$ or $r_{rms}^2 = 2\sigma_{x,z}^2$ as we assume that the distribution is the same in both directions.

For calculation of the deviation in the longitudinal direction σ_y the full width at half maximum (FWHM) of the bunch duration is chosen as $\tau_{FWHM} = 20 \times 10^{-15}$ s. It follows Equation 3.2 where $2\sqrt{2 \cdot \ln 2}$ is the conversion factor between the standard deviation and the FWHM.

$$\sigma_y = \frac{\tau_{FWHM} \cdot c}{2\sqrt{2 \cdot \ln 2}} \tag{3.2}$$

A second driver with uniform distribution in propagation direction and Gaussian distribution in x- and z-direction was generated for comparison. The length Δy of the distribution was chosen, so that the standard deviation $\sigma_{y,\,\text{uniform}}$ is identical to σ_y from the Gaussian driver, resulting in $\Delta y = 2\sqrt{3} \cdot \sigma_y$.

Momenta are derived from the mean kinetic energy E_{kin}. Three different values from 250 MeV to 350 MeV are simulated and compared in this thesis. For all simulations a normal distribution of the energy with a FWHM of 10 MeV is assumed. The total momentum for each particle is now calculated with Equation 3.3.

$$|p| = \frac{E_{kin}}{c} \tag{3.3}$$

This is a simplification of the relativistic energy-momentum relation where the rest mass is neglectable ($m_e c^2$ is only around 0.5 MeV which is an order of magnitude smaller than measurable FWHM).

How much the momentum distribution spreads from the forward propagation axis is given by the pointing angle θ, thus a distribution in spherical coordinates is appropriate. The standard deviation of the pointing angle, the so-called divergence, is set to $\sigma_\theta = 1.6$ mrad.

In experiments this value is only calculated for the divergence towards either the x or z axis, so a factor $\sqrt{2}$ must be multiplied (both directions are assumed to have the same divergence) before it can be used as the standard deviation for the normal distribution of θ. The polar angle ϕ is uniformly distributed over all particles, as the divergence is symmetric around the p_y-axis. Finally, the particle momenta are calculated by transforming from spherical to Cartesian coordinates (Equation 3.4).

$$p_x = \sin\phi \cdot \sin\theta \cdot |p| \qquad p_y = \cos\theta \cdot |p| \qquad p_z = \cos\phi \cdot \sin\theta \cdot |p| \tag{3.4}$$

With the phase space of position and momentum defined for all particles, we can fully describe a particle bunch after the LWFA stage moving close to the speed of light through vacuum, as shown in Figure 3.1a and b.

Next our beam needs to be prepared for the PWFA stage by transmitting it through vacuum until it hits a metal foil. The beam positions are updated by moving the bunch uniformly
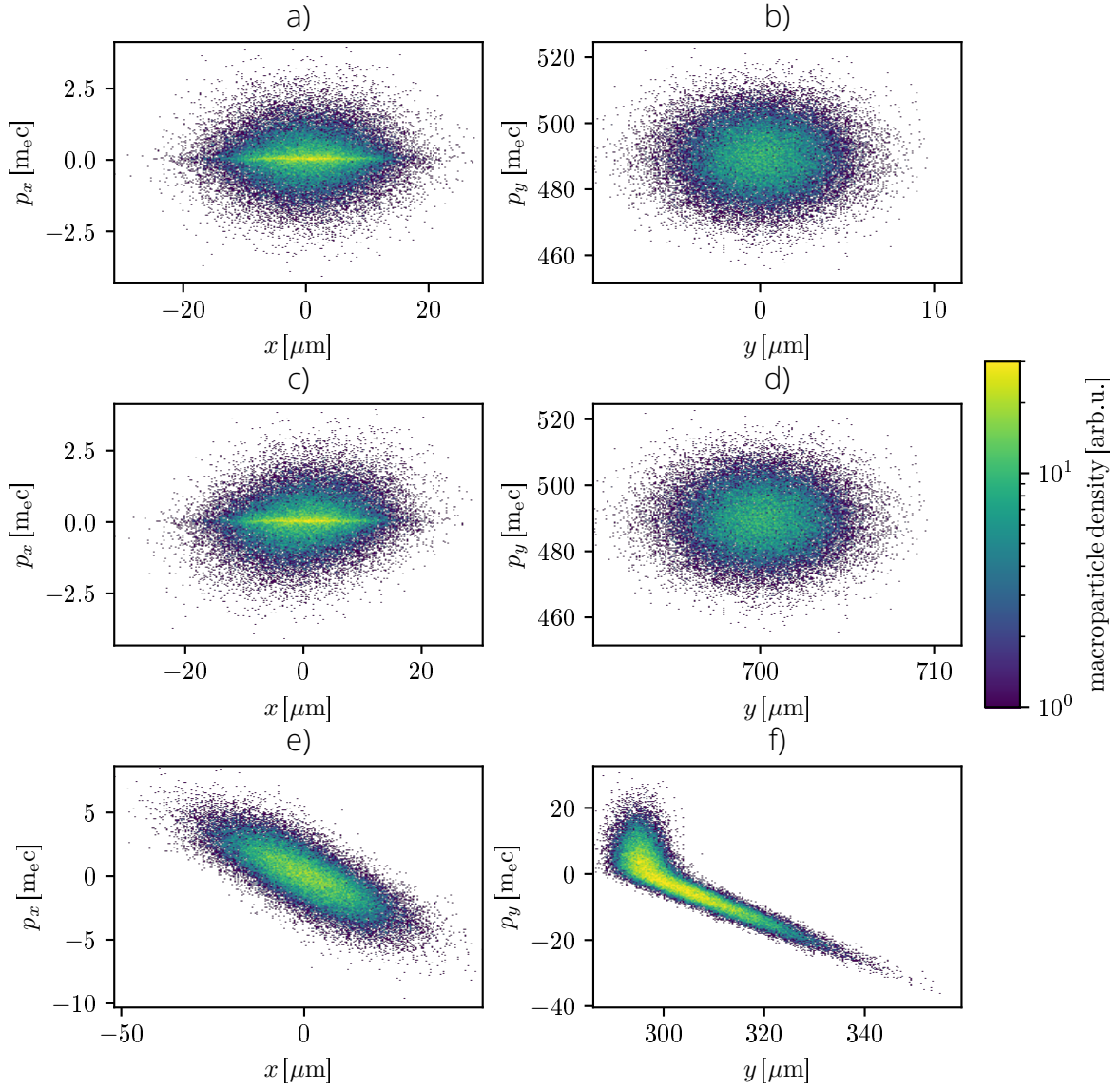
Figure 3.1.: Macroparticle density in phase spaces. **(a)** and **(b)** After leaving the LWFA stage. Transversal momentum is two orders of magnitude smaller than for the longitudinal direction. **(c)** and **(d)** After vacuum propagation. Particles with a higher momentum in x- respectively y-direction moved to the right while slower particles fell behind to the left, resulting in a slight shearing in the phase space. **(e)** and **(f)** After back evolution as a preparation for the acceleration phase. As time was reversed, particles with positive momentum now moved to the left.

through the vacuum without applying forces. This introduces a shear between positive and negative momenta in the phase spaces for all directions, as can be seen in Figure 3.1c and d. Our metal foil is positioned 700 μm after the LWFA gas. In experiment the foil is used to block of the laser from the preceding LWFA stage, with the side effect of scattering the electron beam [26].

To emulate the divergence increase of the metal foil, random noise is added to the momentum in p_x and p_z direction, while the new p_y will be calculated so that the total momentum for each particle is conserved. The standard deviation of the noise normal distribution was chosen so that after the foil, a divergence of 4.2 mrad is achieved, comparable to real experiments [7]. Additionally, drivers with divergences of 1.7 mrad and 8.7 mrad were simulated for comparison; values which are way lower, respective higher than in experiment.

The resulting particle bunch has now the wanted position and momentum that could originate from an ideal LWFA. As the corresponding electric and magnetic fields are created by the PIC-cycle, the condition of the bunch before the acceleration of the acceleration pusher must be computed. The acting force is constant, so simply applying Newtons equations of motion for the same number of timesteps as the pusher returns the bunch in the wanted state. The phase space diagrams of the backwards computed bunch can be seen in Figure 3.1e and f. Notice, that the y-momentum is now centered around 0.

For correct field calculations, it was assumed that the bunch needs to move at non-relativistic speeds, else nonphysical fields could be produced. During tests for this thesis, it was demonstrated that this precaution step was not necessary.

At last, the bunch is placed inside the simulation box. In x- and z-direction it should be in the middle in the box, while being put closer to the front end in y-direction, so no particles fall so far behind, that they leave the box when moving. The simulation can now be run on this synthetically generated bunch.

3.3. Plasma parameters

After the acceleration phase (subsection 2.2.4), our bunch can now enter the plasma, also called gas jet. Only electrons are explicitly added as particles, the corresponding ions are emulated from the field solver. It expects a neutral plasma, so a positive background charge is added. In this case, our plasma is already defined as completely ionized. The density function as seen in Figure 3.2a is separated in multiple regimes starting in the vacuum ($\rho = 0$).

A super-Gaussian density profile (Equation 3.5) is than used to approximate a smooth transition into the plateau where our density ρ stays constant at $\rho_0 = 4 \times 10^{18}$ cm^{-3}. Comparable values for the mean density can be found in experiments [6, 7].

$$\rho = \rho_0 \exp\left(-\left(\frac{y - 6\sigma}{\sigma}\right)^6\right) \tag{3.5}$$

The here assumed constant plateau is an idealization of the small density fluctuations in real plasma.

Generally in all simulations, the driver traversed in the plateau for over 6 mm, where the blowout regime of the wakefield ended for all drivers. As real experiments do measurements on the driver after leaving the gas jet, a second density function was defined were the plateau ends after 3 mm, as in experiments, again with a super-Gaussian transition to vacuum, as seen in Figure 3.2b. This allows us to produce results that can be verified in actual experiments.
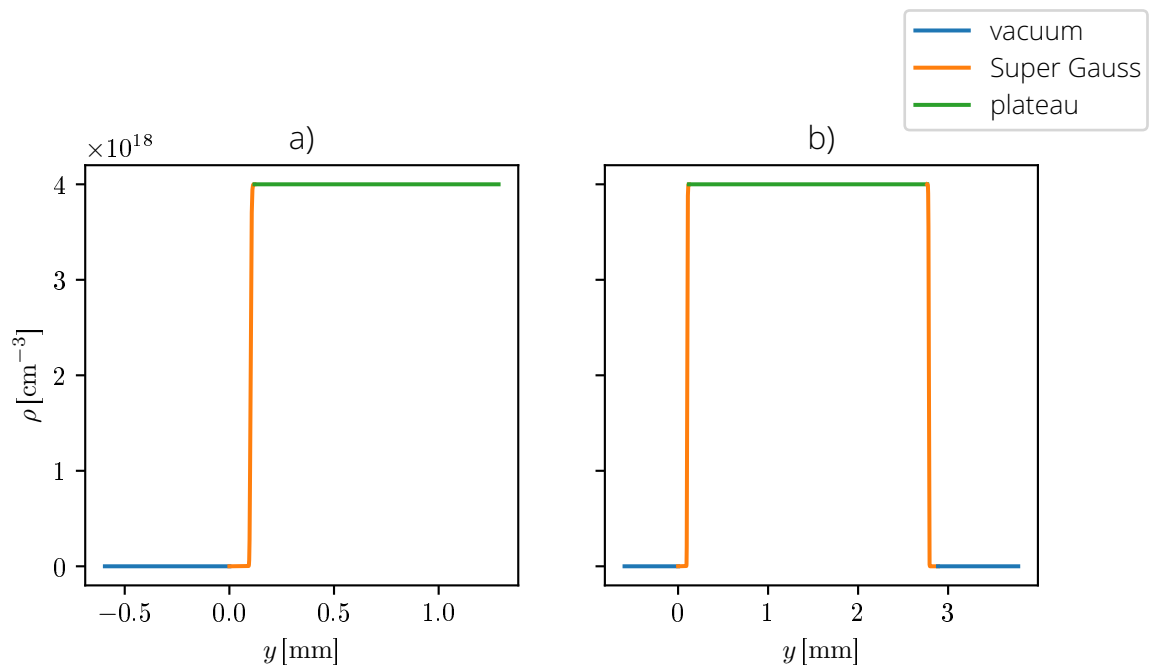
Figure 3.2.: The electron density plotted over the propagation direction. A super-Gauss distribution is used as a transition between vacuum and the density plateau. **(a)** After an initial vacuum, an infinitely long gas jet is described as a constant plateau. **(b)** In contrast to a), the plateau ends after 3 mm and density drops down to 0. This makes results comparable to real experiments.

4. Analysis of the bunch characteristics

In this thesis, the analysis of the bunch and the resulting wakefields are split into two parts. In section 4.1 the change of the spatial charge distribution of the driver is discussed as well as its effect on the quality of the produced wakefield. The latter is quantified by the maximal gainable energy for a potential witness beam.

The second part in section 4.2 focuses on the energy distribution of the driver, especially on changes to the peak energy, as larger changes would violate the assumption of constant peak energy over the course of the PWFA, made in experiments [7].

In both sections, analysis is initially done for a driver with Gaussian charge distribution, an initial kinetic energy of 250 MeV and a divergence of 4.2 mrad. This driver is then compared to drivers with different charge distributions, initial energy or divergence, highlighting the effects on the created wakefield.

Many figures in this chapter show a spatial distribution in the ζ-z-plane. ζ is an axis that moves at the speed of light parallel to the driver bunch. It is defined as $\zeta = y - ct$ with the speed of light c, time t and propagation axis y. The y-coordinate has the meaning of the distance of the bunch from the start of the plasma and is given in the description of the figures. The connection of the coordinates is also depicted in Figure 4.1.

4.1. Transformation of the driver distribution

In this section, the movement of driver-particles is discussed and the changes of their position with respect to each other are shown. As such tracking of individual particles is not possible in experiment, this will give further insight into the effects of the PWFA on the drive beam. Additionally, the created wakefields are analyzed with respect to their formed electric fields and the energy a potential witness can gain from these fields.

In Figure 4.2 a time series of 2D histograms, showing the charge density of the driver after entering the plasma, can be seen for the ζ-z-plane, with ζ being the axis, which moves with the driver bunch. Also given is y, the distance to the start of the plasma upramp.

A log scale is chosen to make the borders with low density visible. Additionally, the Lorentz force is layered over the histogram to visualize the cause of the transformation of the driver. It is retrieved from the $\vec{E}$- and $\vec{B}$-field, that every macroparticle stores. The window is then separated into bins and for every bin the mean force on the macroparticles was calculated and plotted as a force field, with the color of the lines quantifying the absolute force. This is
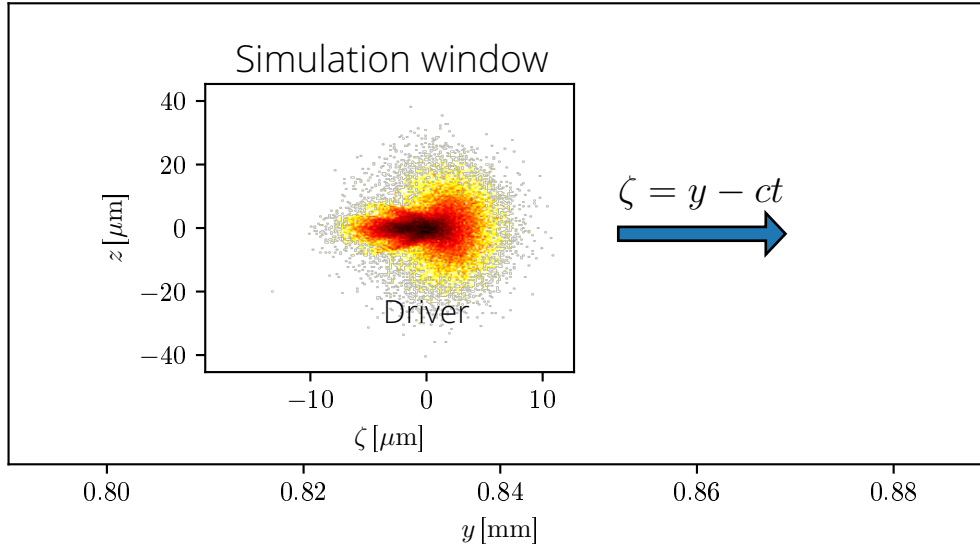
Figure 4.1.: Relation between the co-moving coordinate ζ and the traversed distance y. The position of the driver is constant in ζ as the axis moves with it.

similar to the perspective, that there is one macroparticle per bin and the force acting on this particle is plotted.

At start, the spatial distribution still follows a 2D Gaussian distribution, as seen in section 3.2. After the driver propagated for 0.3 mm through the plasma, the first cavities start to arise. The focusing Lorentz force of these cavities forms a tail at the end of the driver while the cavities are still in the linear regime. Only small forces act on the front of the beam, so that the front part can diverge freely. In the center and back of the driving bunch are great forces, pushing the particles back and simultaneously centering them, resulting in the creation of a tail. These forces result from the formation of the first cavity behind the driver. As can be seen in Figure 4.3b, the nearest cavity forms directly behind the center of the driver so the backside already experiences the decelerating and focusing fields of the cavity. Comparing the length of the beam over time (see vertical lines in Figure 4.2) shows that the tail is not an elongation of the driver backwards but the backside experiencing focusing forces, which are narrowing the backside. Cavities in blowout regime form with the same width as the tail of the driver and widen when the tail spreads apart.

The focus forces at the back of the driver cause the electrons to overshoot. This results in a widening of the tail and the formation of wing-like structures. The cavities also start to widen and form the strongest electric fields of the whole PWFA stage during this process. The formed wings are diverging while new wings form behind them by particles which oscillate as they got pulled back by the focusing force, causing them to overshoot again. This forms a chain of smaller wings, all spreading with time and broadening the tail further. In this stage, the strength of the electric fields in the cavities already decreases while the electron density in the wakefield rises.

The backside of the driver spreads further as particles from the wings leave the cavities and therefore the impact of the focusing fields. This causes the backside to grow in transverse direction together with the front of the bunch. Meanwhile the $\vec{E}$-fields of the wakefield reduce in strength and the cavities are flooded by electrons again. The blowout regime goes over into the linear regime, as seen in Figure 4.3d. Still there are strong forces acting on the center of the bunch, causing it to lose energy. The discussion of this energy loss is continued in section 4.2, for now we only look at the distribution of these particles.
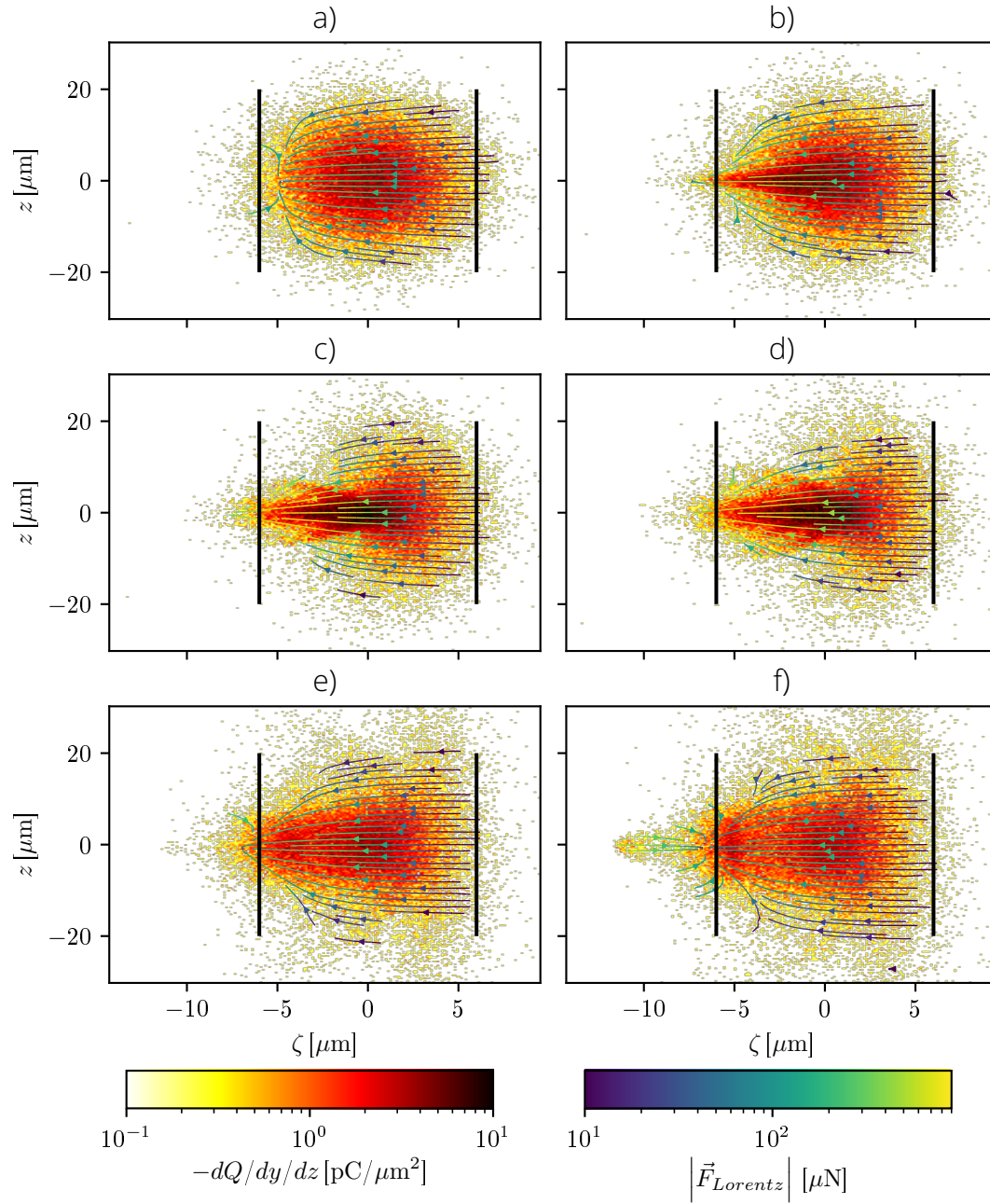
Figure 4.2.: Time series of a charge density histogram of the driver electrons integrated over the x-axis in Log scale. The acting Lorentz Force is drawn on top as vector lines. Vertical lines are drawn to make changes in length of the bunch better visible. The histogram is plotted in the ζ-z plane, with ζ being a co-moving coordinate axis. The distance y traversed in the plasma is given. **a)** ($y = 0.04\,\text{mm}$) When entering the plasma. Still a Gaussian distribution, weak focus forces at the backside. **b)** ($y = 0.36\,\text{mm}$) Formation of the tail from focusing forces. Decelerating forces grow. **c)** ($y = 0.76\,\text{mm}$) First wing spreads from the tail. Strong decelerating forces on the backside. **d)** ($y = 1.08\,\text{mm}$) More wings emerge and spread. Still strong decelerating forces. **e)** ($y = 2.90\,\text{mm}$) Shortly before bunch breakup with visible elongation of the bunch. Only weak forces remain. **f)** ($y = 3.38\,\text{mm}$) Bunch after breakup. The fallen back part gets accelerated from the backside of the first cavity.
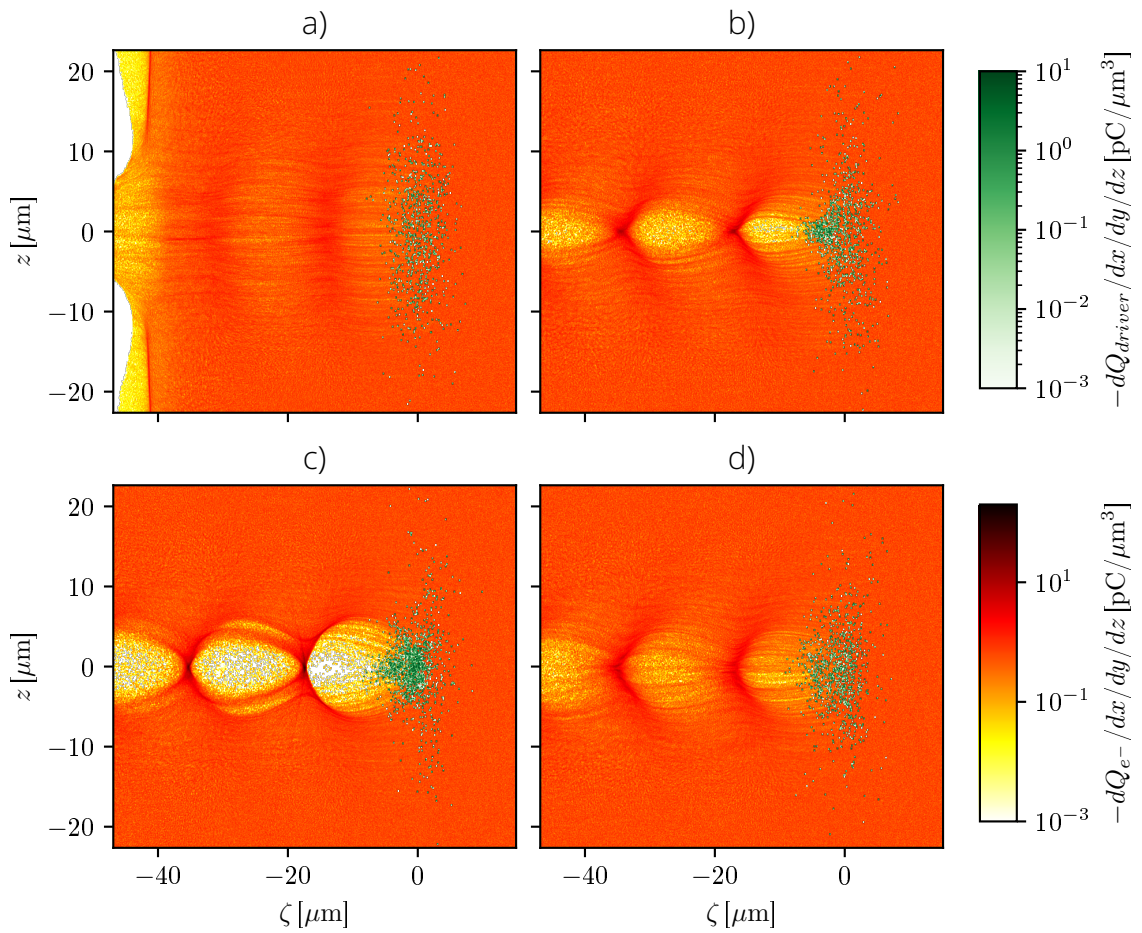
Figure 4.3.: Time series of the charge density of the plasma and the driver at $x = 0$ over co-moving ζ and z. **a)** ($y = 0.04\,\text{mm}$) After entering plasma. The vacuum can still be seen on the left border. Weak cavities can already be seen. **b)** ($y = 0.36\,\text{mm}$) Cavities forming together with the tail of the driver. **c)** ($y = 0.68\,\text{mm}$) Blowout regime during spread of the wings on the backside of the driver. **d)** ($y = 2.27\,\text{mm}$) Wakefield returns to linear regime before bunch breakup.
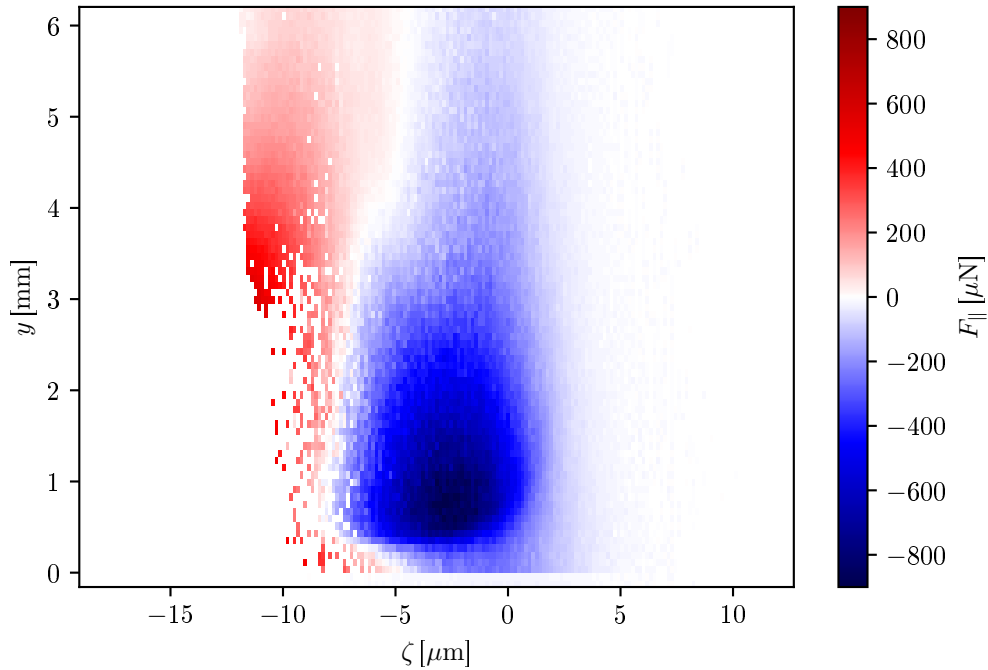
Figure 4.4.: Histogram of the longitudinal part of the Lorentz force. The force is sampled over the co-moving ζ-axis at a slice in the middle in z-direction for every 2000 timesteps. This slice here is plotted over y, the distance of the driver from the start of the plasma, showing how it changes in position and strength.

In Figure 4.4 the strength and position change of the longitudinal Lorentz force can be seen over the traversed distance y. It shows how the force pushing the driver back first builds up and then loses its strength after the maximum at 1 mm. A forward pushing force on the backside of the driver can also be seen, as the Gaussian distribution of the driver reaches so far back, that some particles are positioned in the accelerating part of the first cavity. Notable is the situation around $y = 3$ mm, where the bunch collapses and particles start to fall back rapidly, so they get accelerated again in the back of the first cavity. These particles stem mostly from the middle of the driver, where the strongest backwards-pushing forces acted before and caused them to drain their energy.

Here the bunch breakup has no big effect, as the cavities already resumed to the linear regime and only a small part of the driver did fall back. Only small forces remain to act on the driver, so it slowly diverges to the transverse sides.

4.1.1. Particle tracking

To support the claims made about the particle movement, particle tracking was used. In Figure 4.5a the particle distribution, shortly after entering the plasma, can be seen. The colors show the co-moving ζ-position of the respective particles after the bunch breakup. Driver electrons which fall behind during the bunch breakup originate from a small region right behind the center of the bunch. As seen in Figure 4.2, this is the region where the strongest Lorentz force acted. The ζ position change of other particles is neglectable small, as only weak forces act.

Additionally in Figure 4.5b the middle slice of this distribution was captured every 2000 timesteps and plotted over the traversed distance y. The fallback of the particles in the middle
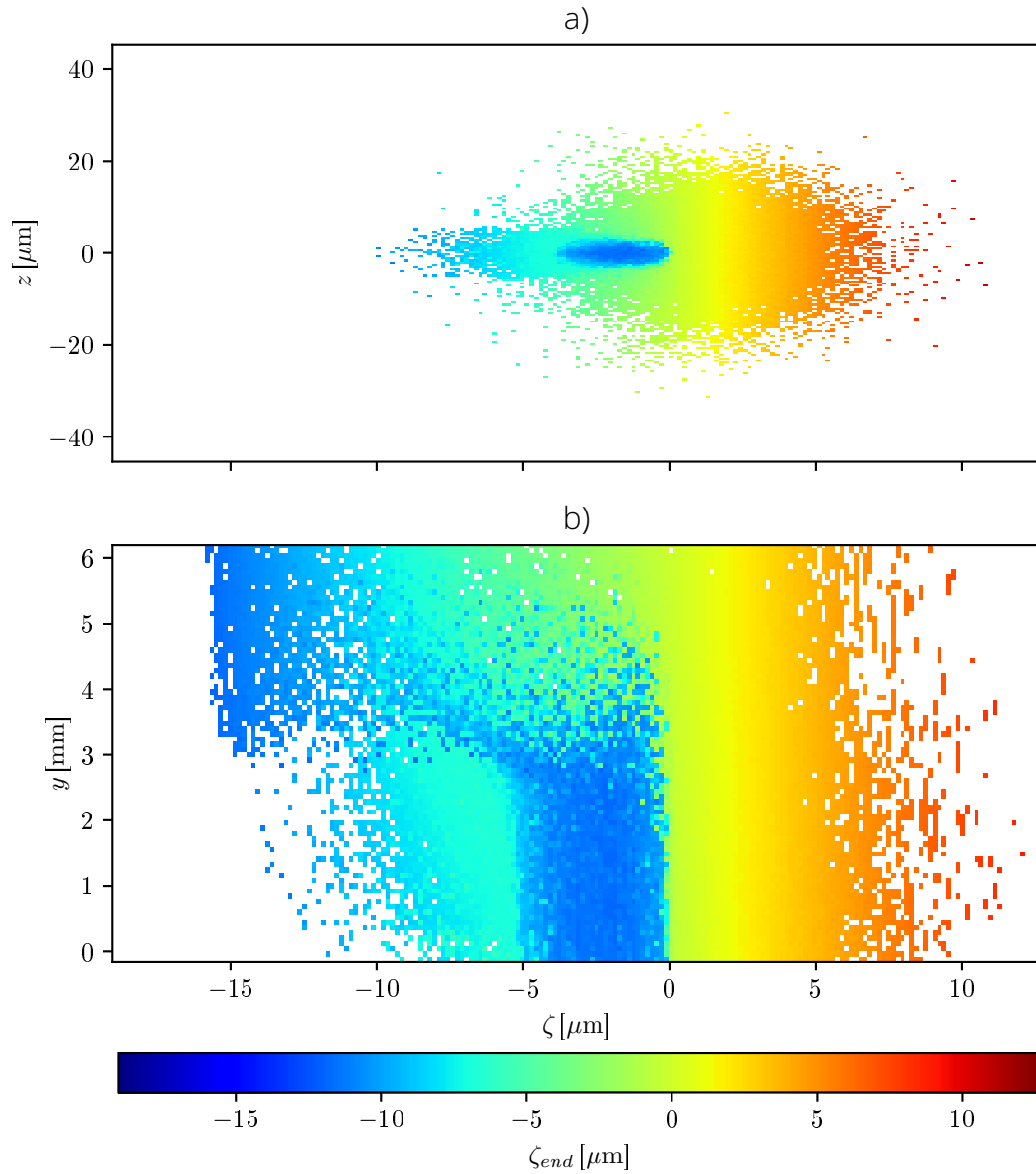
Figure 4.5.: Position of the particles in bins after bunch breakup. Each bin shows the minimal ζ-position (co-moving position) of the particles in it to visualize how it will move over time. **a)** 2D distribution of the bins for $y = 0.60\,\mathrm{mm}$. The blue particles in the middle will fall back to the backside of the driver with time. **b)** The bins centered at $z = 0$ are sampled every 2000 timesteps and plotted over the traversed distance y in the plasma. Around $y = 3\,\mathrm{mm}$ the particles in the middle falls behind.
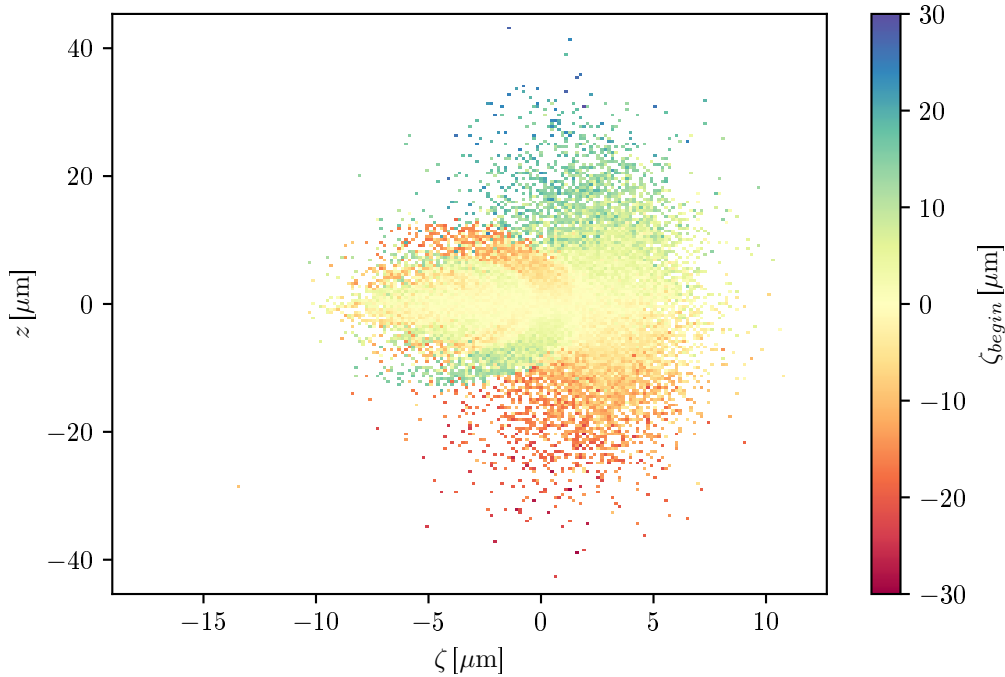
Figure 4.6.: z-positions of the particles before entering the plasma plotted over their current position ($y = 1.31$ mm). Each bin represents the mean z-value at a timestep. In the back of the driver, particles from below and above $z = 0$ alternate.

during bunch breakup can clearly be seen.

The same tracking was done for the z-direction, seen in the time series in Figure 4.6. As the movement in z-direction is symmetric, this results in bins with equal number of particles from the top and bottom half to be displayed as yellowish white, thus the transition of particles from top to bottom and reversed can not be seen. Still, the effect is clear as the wings can clearly be seen at the end of the driver. The alternating colors can be explained by the oscillation of the electrons, as they get pulled back to the center and form smaller wings. No such motion is observed in the front part in the driver.

4.1.2. Parameter comparison

The transformation of the driver beam shape and subsequent changes of quality of the wakefield were compared for different initial parameters. To quantify the wakefield quality, the maximally gained energy for a potential witness beam is considered. In Figure 4.7 the charge distribution and longituduinal direction $E_\parallel$ (accelerating and decelerating) of the electric field of the plasma electrons are compared over time.

In a), a change in width of the cavities can be observed, an effect that was measured in experiment [7]. A witness beam which is phase locked with the driver, meaning it is constant in ζ, would therefore not get maximal energy gain when placed at a position where the accelerating field is maximal as it would later experience a decelerating force, when the cavities shrink again. In b) this is visible, as the decelerating blue field moves to the right over the position of the strongest red accelerating field. Drawn in is also the expected energy gain for a potential witness beam. This gain was calculated by integrating the Lorentz Force, created by the fields, over the traversed distance. The peak is not over the position with the highest
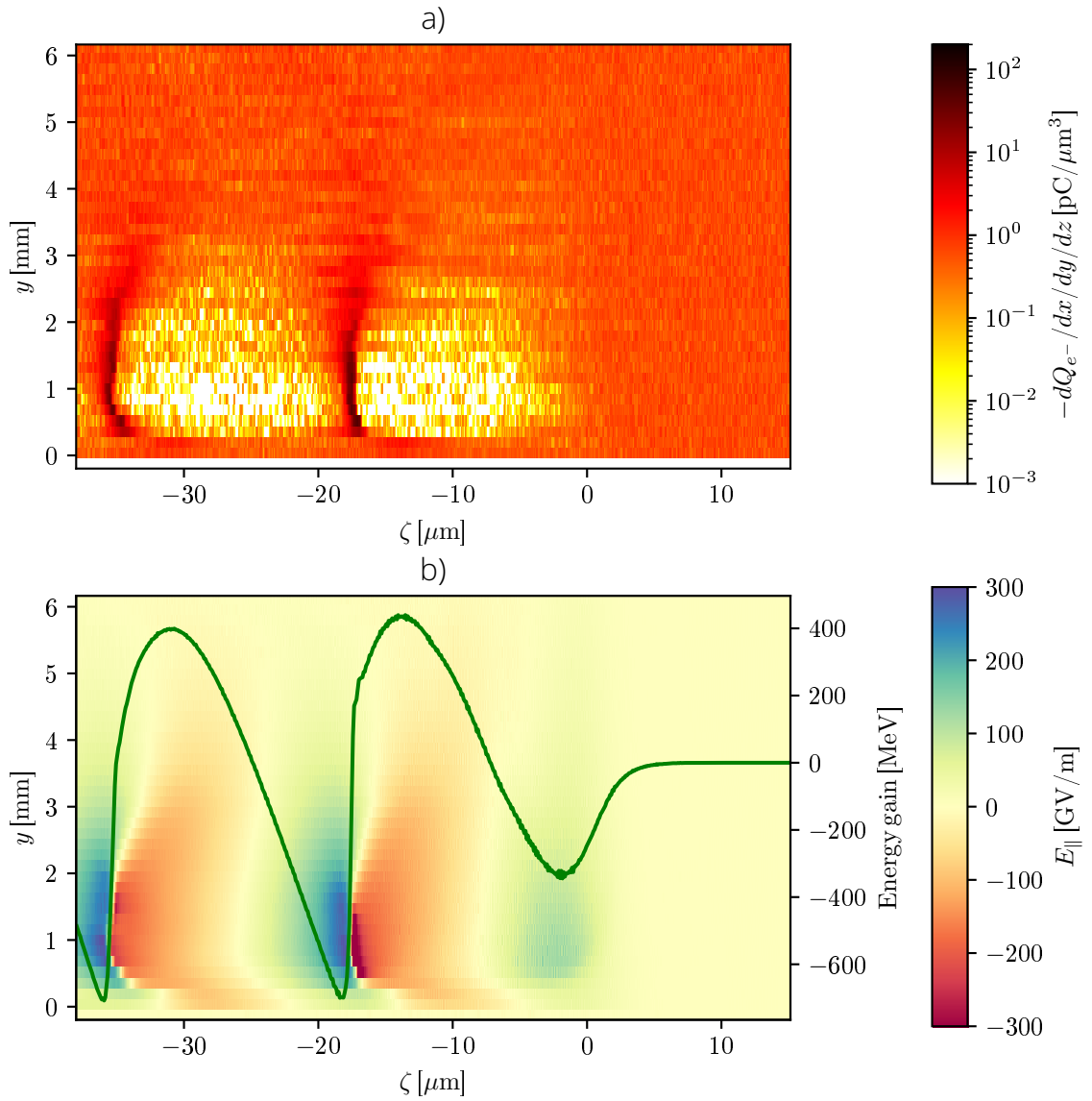
Figure 4.7.: **a)** The charge distribution at the co-moving ζ axis with $x = z = 0$ is plotted over the distance in the plasma y. Clearly visible is a change in the width of the cavities after $y = 2$ mm. **b)** The electric field in co-moving ζ direction for all grid points at $x = z = 0$ is plotted over y. As a green line, the gained energy for a theoretical witness beam is plotted over ζ too.
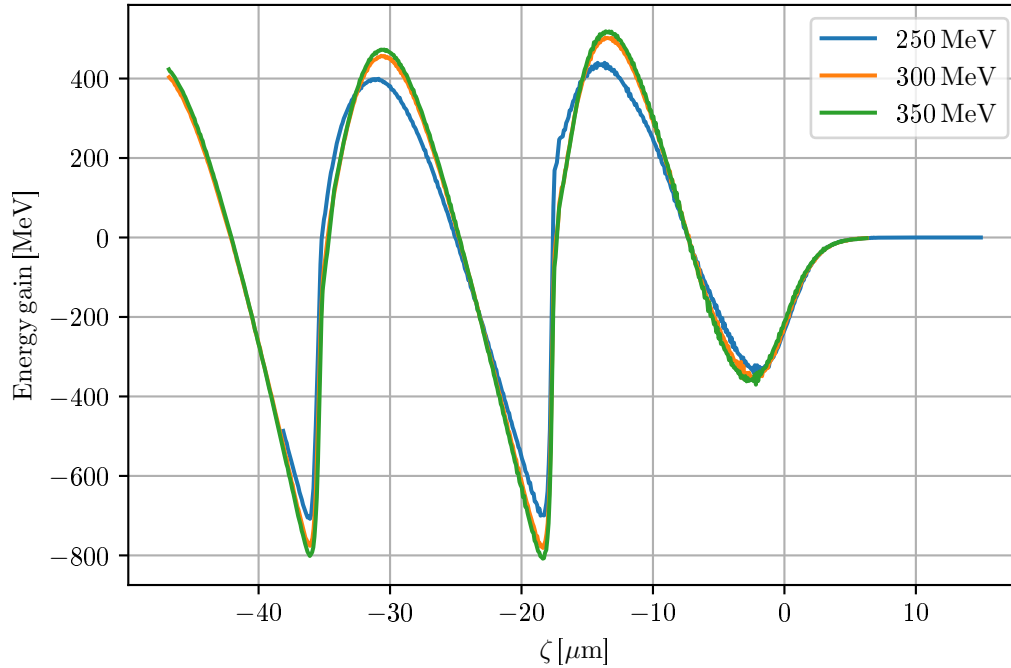
Figure 4.8.: Witness energy gain for three different initial kinetic energies of the driver.

field but at the position where the highest field is after the cavities shrank. This maximum of gained energy can now be used to compare the wakefields for different drivers. Effects of the hypothetical witness beam on the wakefield, like beam loading [27, 28], are not considered in this discussion.

Energy comparison

A comparison between different initial mean kinetic energies of the drivers with same divergence was made. We compare the three energies 250 MeV, 300 MeV and 350 MeV under the aspect how much more witness energy can be gained with higher initial bunch energy. Only small qualitative differences exist in the wakefields between the three energies. Generally, the blowout regime can be achieved over a longer distance for higher energy drivers. This results in slightly increased energy gains, as seen in Figure 4.8. The maximally gainable energies can be found in Table 4.1.

E_{kin} [MeV]	E_{gain} [MeV]
250	439.7
300	502.6
350	518.9

Table 4.1.: Maximally possible energy gain for different initial kinetic energies.

While the jump from 250 MeV to 300 MeV results in 63 MeV higher gains, there is a diminishing return, as only 16 MeV more are reached when increasing from 300 MeV to 350 MeV. Real experiments are restricted by the length of the plasma jet. This results in an even smaller witness energy increase, as the main difference between the three PWFA runs is the longer
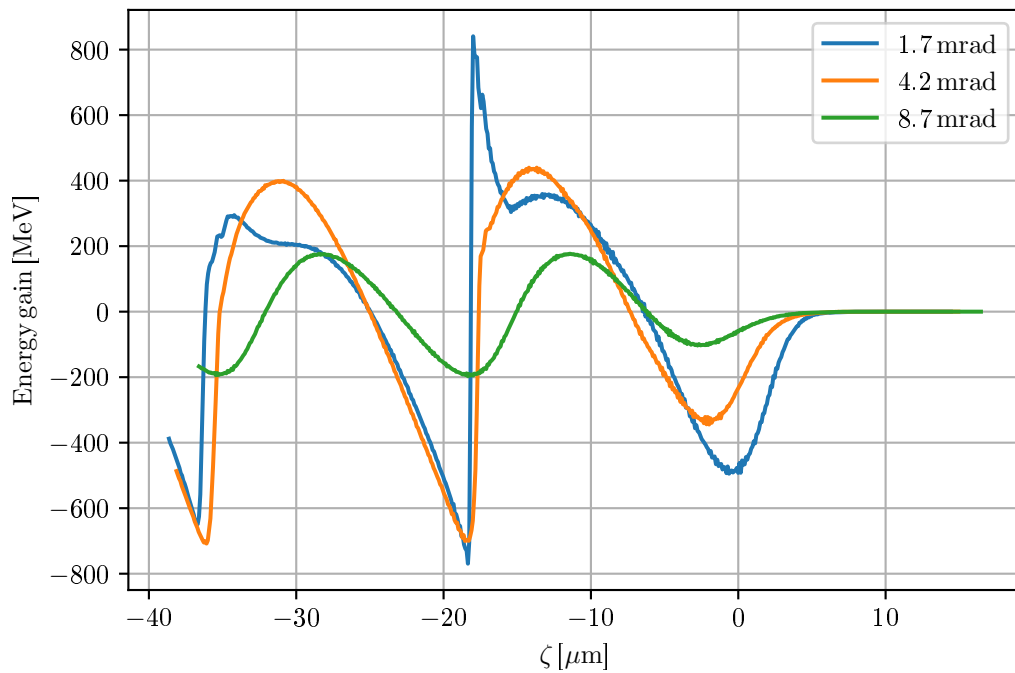
Figure 4.9.: Witness energy gain for three different initial driver divergences.

duration of the blowout regime for higher energy drivers. Therefore, there may be no need for higher energy drivers, as the advantages vanish. The values make also apparent, that there are only small differences in the energy loss behind the driver (minimums at −3 μm in Figure 4.8). The driver with higher energy lives only longer because it has more energy to lose, not because it loses less per time.

Divergence comparison

Next, the driver qualities for three different divergences after passing the metal foil were compared. The energy gains over ζ for a high divergence ($\sigma_\theta = 8.7$ mrad), middle divergence ($\sigma_\theta = 4.2$ mrad, as seen in experiments) and low divergence ($\sigma_\theta = 1.7$ mrad) beam are shown in Figure 4.9. For all curves at least one maximum, like in the graphs before, can be seen per cavity. Additionally, there is a second much higher peak for the low divergence curve at the position, where the backside of the cavity was during blowout. This peak results from the long-standing blowout with extreme fields and the following smaller blowout, caused by the remaining driver, as seen in the charge density graphs Figure 4.10.

Even before the cavities fill and a linear regime sets in, the driver breaks up as the strong forces cause fast energy drain (see the high energy loss in the first minimum behind the driver in Figure 4.9. Through beam loading, the energy of the wakefield was absorbed by the fallen back part of the driver, causing the cavities to transition into the linear regime. Still there remains a small blowout behind the fallen back driver, caused by its high charge density. The peak of the energy gain is positioned in this smaller wakefield.

For a driver with high divergence, no blowout is achieved so the wakefield remains in the linear regime with weak electric fields. These weak fields are not able to cause a bunch breakup, resulting in the bunch just diverging with time. The resulting maximally gained energies can be found in Table 4.2. While the normal maximum is highest for the 4.2 mrad driver, the second
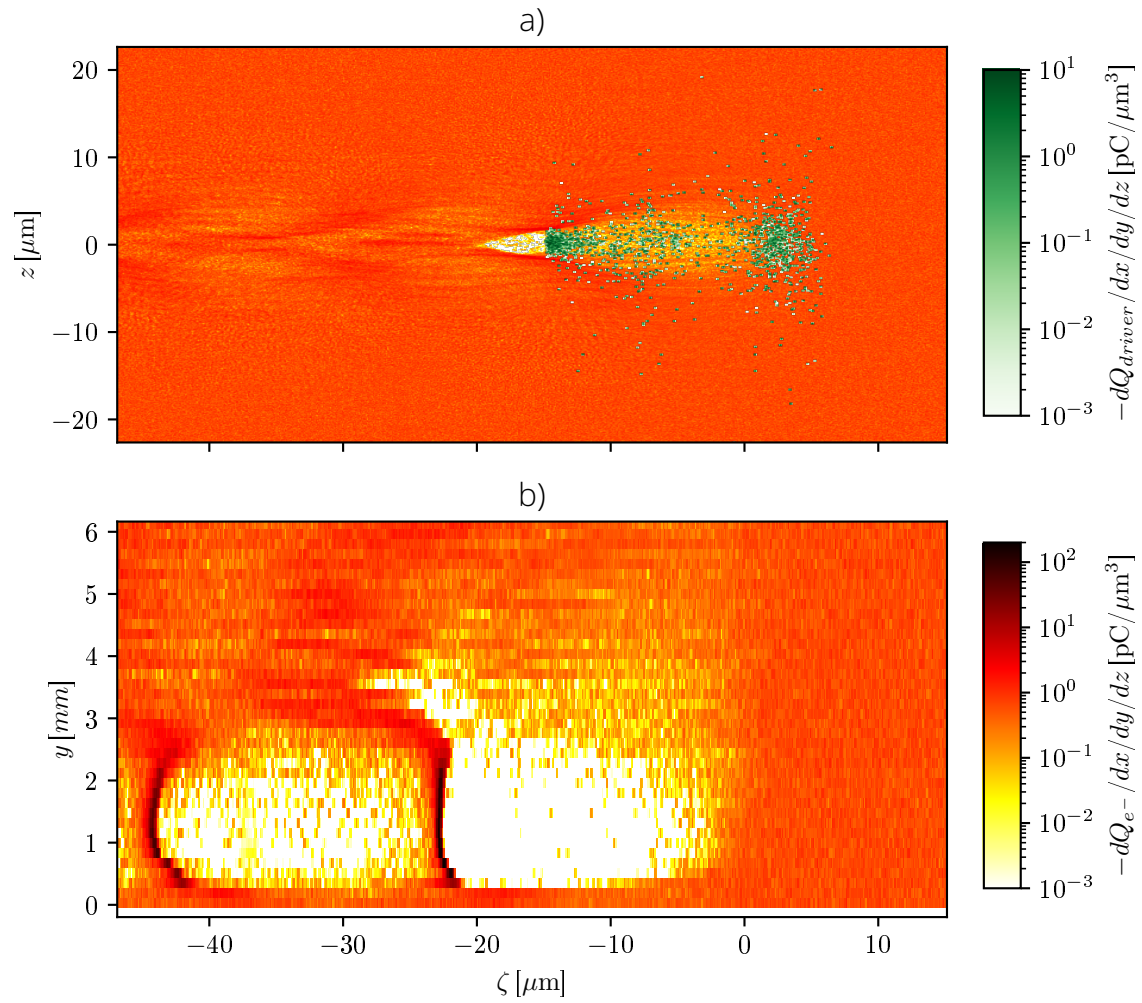
Figure 4.10.: Charge density of driver and plasma for a low divergent driver for different time steps. **a)** ($y = 3.22$ mm) Charge density histogram showing a small cavity forming behind the broken up part of the driver. **b)** Charge density slice of the centered grid points plotted over y.

σ_θ [mrad]	E_{gain} [MeV]
1.7	359.3
1.7 (sec. peak)	840.7
4.2	439.7
8.7	176.9

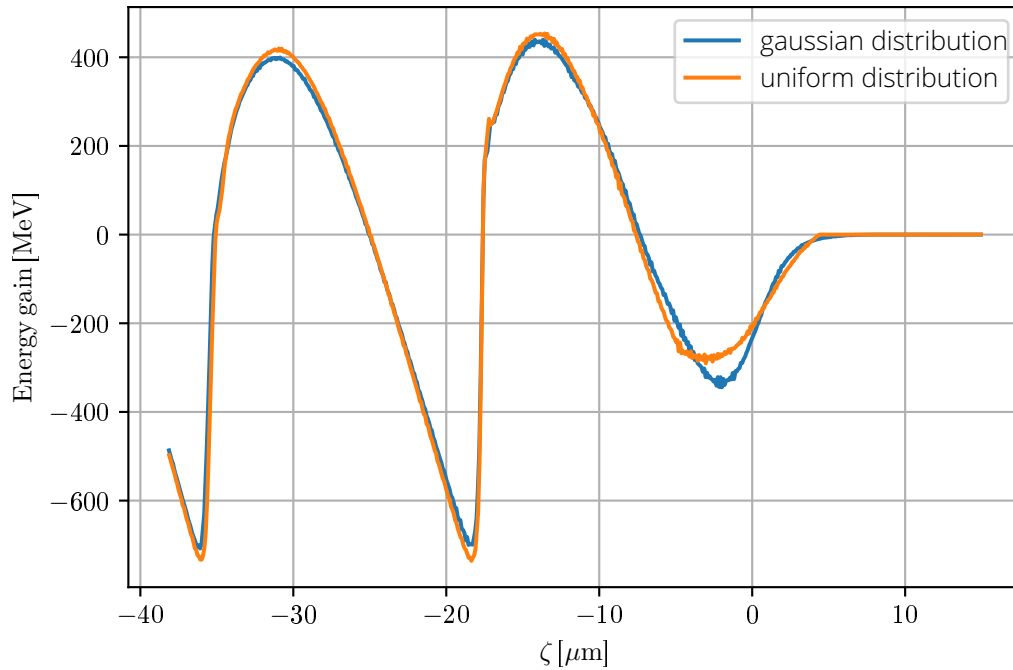Table 4.2.: Maximally possible energy gain for different initial divergences.

Figure 4.11.: Witness energy gain for two different initial charge distributions.

maximum of the low divergence driver achieves nearly double the energy gain, giving good reasons to strive for low divergent beams.

The question arises, why the change in divergence causes such an extreme difference for drivers. It is possible that, that a higher current is induced from the low divergence driver. The velocity in propagation direction is higher and the spatial distribution is denser, as the particles do not diverge as much before entering the plasma, causing a higher current.

Distribution comparison

Even though in the experiment, the shape of a driver beam is hard to control when leaving the LWFA towards the PWFA, a comparison between different distributions can give new insights into the properties that are needed from a driver to form high accelerating fields. Besides the driver with Gaussian distribution in all spatial direction, a driver with Gaussian distribution in transverse direction and uniform charge distribution in propagation direction was simulated.

The energy gain graph Figure 4.11 shows that only a small win of 14 MeV in maximal energy can be achieved compared to the Gaussian driver. The biggest difference in the two curves lies in the higher minimum positioned at the backside of the driver, that results in smaller energy loss and therefore a 0.7 mm longer traversed distance before breakup.

Figure 4.12 shows a timeseries of the uniform driver. When compared to Figure 4.2, the similarity in the transformation is visible. The formed tail does not get as thin as for the fully Gaussian driver, as the overshoot happens before the outer particles reach $z = 0$. Still the uniform driver survives longer before breakup, caused by the weaker decelerating forces, as seen in the higher minimum in Figure 4.11.

4.2. Peak energy shift

In this chapter, the change in energy of the PWFA driver is discussed, as this gives further insights into its stability and therefore also the stability of the wakefield. In Figure 4.13a the change of the energy distribution over time can be seen for the 250 MeV, 4.2 mrad Gaussian driver. When inducing the wakefield, the Lorentz force created by the fields of the first cavity acts on the driver causing it to lose energy. As only parts of the driver experience this force, the energy distribution is not moving to lower energies entirely, but instead spreading. The plot shows the growth in low energy electrons until $E = 0$ is reached, visualized by the E_{min} curve. In blue, the mean is also plotted, showing how it reduces with time. Also the maximum energy E_{max} is shown, which increases. This increase stems from the particles, which gain energy as they are so far back in the bunch, that they get pushed by the Lorentz forces in the middle of the first cavity.

Notable is the fact, that the histogram for every timestep is not uniform but has visible maxima and minima in form of the black and yellow stripes in Figure 4.13a. The maximum with the highest energy is called the peak energy, here additionally plotted in green. This energy is important in experiment, as the assumption that it stays constant during the PWFA is used to calculate the initial charge of the driver before entering the PWFA (see [7]). In Figure 4.13b only the peak energy is plotted over time, showing that it is in fact not constant. The peak energy drops from 250 MeV to 244 MeV shortly after entering the plasma. A plateau exists at this energy until bunch breakup, after which the peak further drops.

The systematic uncertainty of the peak energy is given by the size of the bins while the statistical uncertainty results from the uncertainty of the fit.

The fit assumes two summed Gaussian distributions as a simplification of the real distribution, which consists of multiple peaks with different heights and widths as well as an unknown background noise. Only the peak energy and the second peak are fitted. This fit can produce strong outliers during the first half millimeter and still seems to have a slight visual offset to the real curve afterwards, so a better fit method should be used in future studies.

Also drawn is the curve for a simulation with a down ramp for the plasma after 2.7 mm of transverse propagation, as peak energy is measured after leaving the plasma jet in experiment. The drop-off of 5 MeV remains after the downramp and would therefore be measured in experiment, when high enough accuracy can be achieved. Even after the driver left the plasma, the peak energy further dropped. No significant decelerating forces act in this phase, so the loss may just be caused by an inaccuracy of the energy fit.

For this and all following simulations, the peak energy loss was also analyzed for only the particles which do not leave the simulation box. This should prevent an energy loss due to the loss of high-energy particles. No qualitative changes in the peak energy curves were observed. The effect of the particle loss is therefore neglectable.

Currently, the uncertainty on the peak energy measurement in experiments is significantly higher than the 5 MeV jump. Thus, caution is needed when assuming a constant peak energy, especially after bunch breakup.
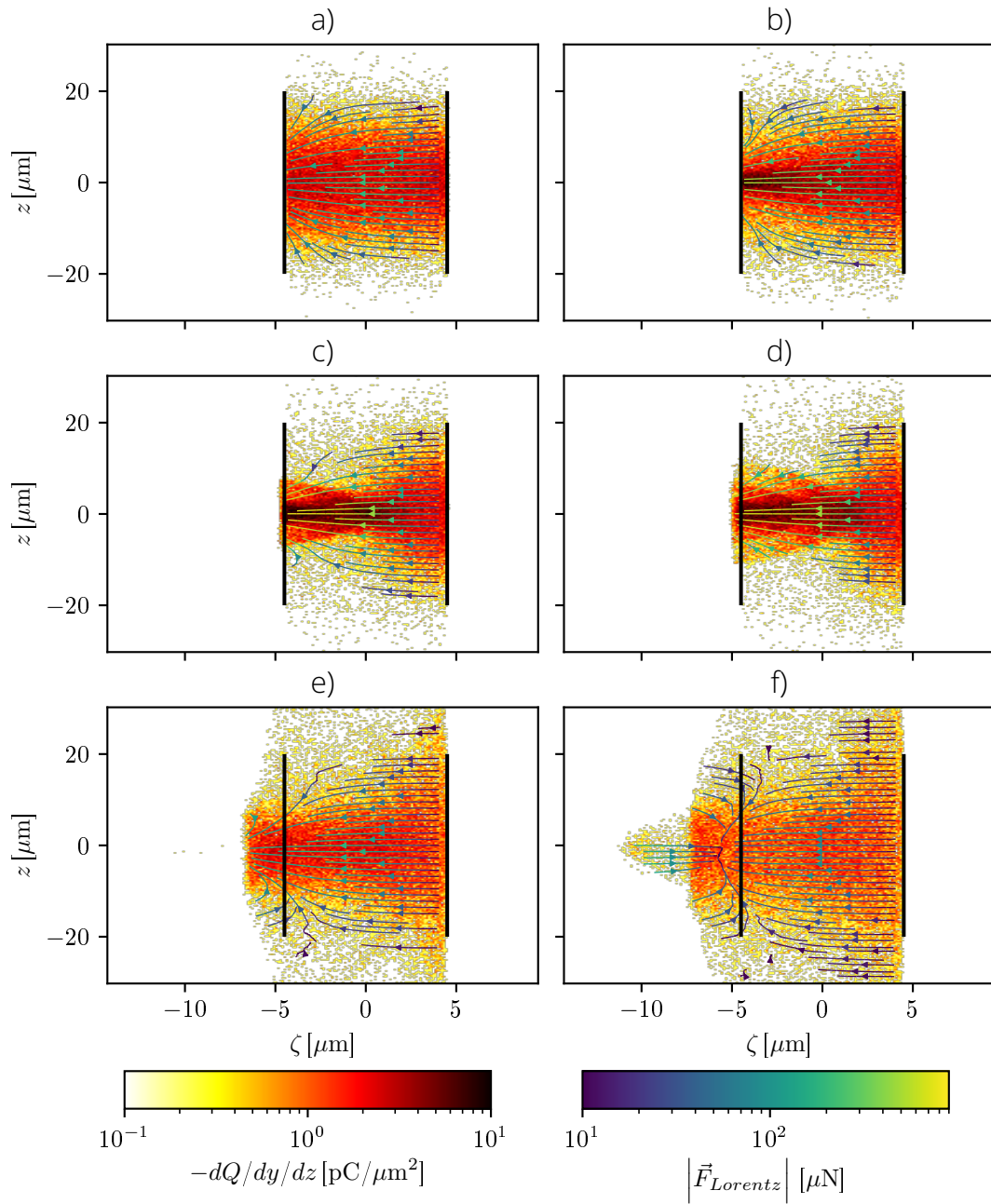
Figure 4.12.: Time series of a charge density histogram of a driver uniform in co-moving ζ-direction, integrated over x, with the acting Lorentz Force drawn on top as vector lines. Vertical lines are drawn to make change in length of the bunch better visible. **a)** $(y = 0.04\,\text{mm})$ When entering the plasma. Still uniform in ζ. **b)** $(y = 0.36\,\text{mm})$ Compared to the Gaussian driver, the tail doesn't get as thin. **c)** $(y = 0.76\,\text{mm})$ First wing spreads from tail. Strong decelerating forces on the backside. **d)** $(y = 1.08\,\text{mm})$ More wings emerge and spread. Driver expends in ζ with higher elongation near the z-center **e)** $(y = 3.54\,\text{mm})$ Shortly before bunch breakup. Note the longer distance before bunch breakup. **f)** $(y = 4.97\,\text{mm})$ Bunch after breakup.
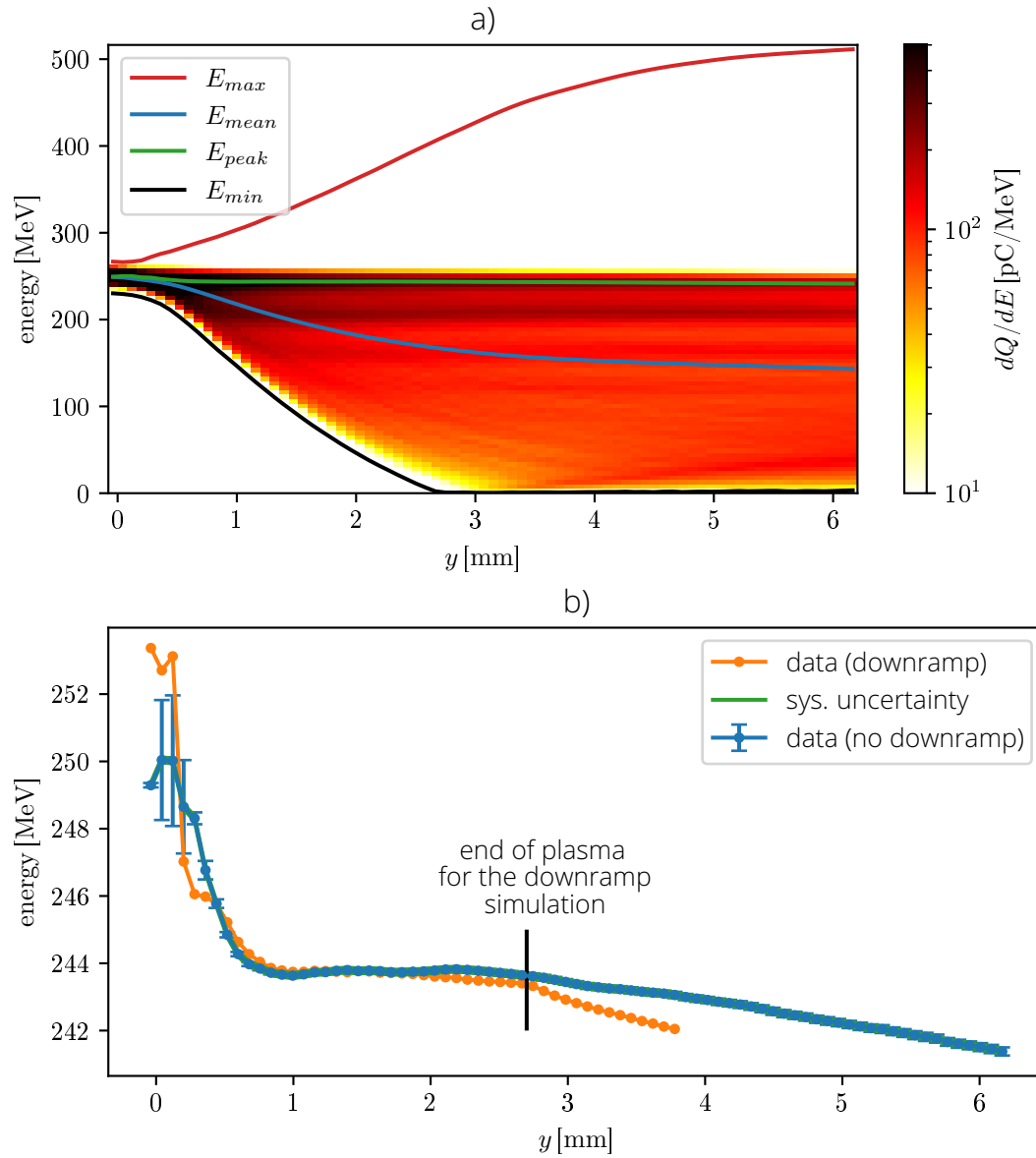
a)

b)

Figure 4.13.: **(a)** Energy histogram over time. A histogram of the charge distribution over the energy is created every 2000 timesteps and plotted here over y. **(b)** Peak energy plotted over y. A second curve for a simulation where the plasma jet ends after 3 mm is drawn in too with the vertical line marking the point of the downramp. Note that the systematic uncertainty range is barely visible behind the curve of the data.

4.2.1. Locality of the energy

The energy loss and spatial locality of the energy peaks can be visualized again by binning the macroparticles in space and analyzing the mean energy in every bin. This mean energy is then plotted over the positions of the bins, an example of this can be seen in Figure 4.14a.

Parts of the bunch, where a strong decelerating force acts, have lost most of the energy while the front part, where only weak forces act, retained the peak energy. The energy loss in the back consists not of a steady gradient but islands with constant energy, as seen by by the big areas with a constant color. The complete time series of the energy is plotted in Figure 4.14b.

Notable is the constant energy in the front half of the driver and the strong energy loss in the middle. When energies around zero are reached, the electrons fall back, where they get accelerated again from the first cavity. Also notable is, that the highest energies are achieved at the back of the driver, where the accelerating part of the cavity starts and pushes the electrons forwards in propagation direction.

4.2.2. Parameter comparison

Energy comparison

These results are again compared to different initial conditions of the driver. In Figure 4.15 the loss of peak energy over traveled distance is compared again for three different mean kinetic energies.

For all energies the initial energy drop of 6 MeV to 7 MeV can be observed, as well as the slower loss of peak energy afterwards. The initial drop-off ends for all energies after traversing the plasma for a distance of 1 mm, with the high energy drivers having bigger energy losses. While the 250 MeV driver has a visible plateau, there are smaller or no plateaus for the other two energies. Still, the energy loss happens slower at the point after the initial drop-off and only increases with advancing distance in the plasma.

The slow energy loss afterwards exists for all drivers. While the difference between the 250 MeV and 300 MeV curve stays roughly the same except for some fluctuations, the difference between the 300 MeV and 350 MeV curve increases with time, meaning that the 350 MeV peak loses its energy faster. The points of bunch breakup are also marked, which seem to be uncorrelated to the progression of the curve.

Even when there is no plateau for higher initial energies, the energy loss beyond the initial drop-off is comparably small before the end of the gas jet in experiments at around 3 mm [7].

Divergence comparison

When the same analysis is done on the different initial divergences, as seen in Figure 4.16, big qualitative differences become apparent. The low divergence driver has the same drop-off as the one with normal divergence but afterwards no further energy loss but instead a small increase of roughly 0.5 MeV can be observed. For the high divergence driver, the initial drop-off is smaller, with only 4 MeV, but afterwards the peak energy decreases linear. After 3 mm the driver already has lost 9 MeV of energy, which is still smaller than the energy uncertainty in experiments [7] but could become relevant in the future.

The remaining fields after bunch breakup of the low divergence driver may be too weak to decelerate the bunch, thus the fields cannot further decrease the peak energy. This would result in the curve depicted above. Meanwhile the linear regime of the high divergence driver is capable of further decelerating the front part of the driver, resulting in a high peak energy loss, as the bunch never breaks during the simulation time.
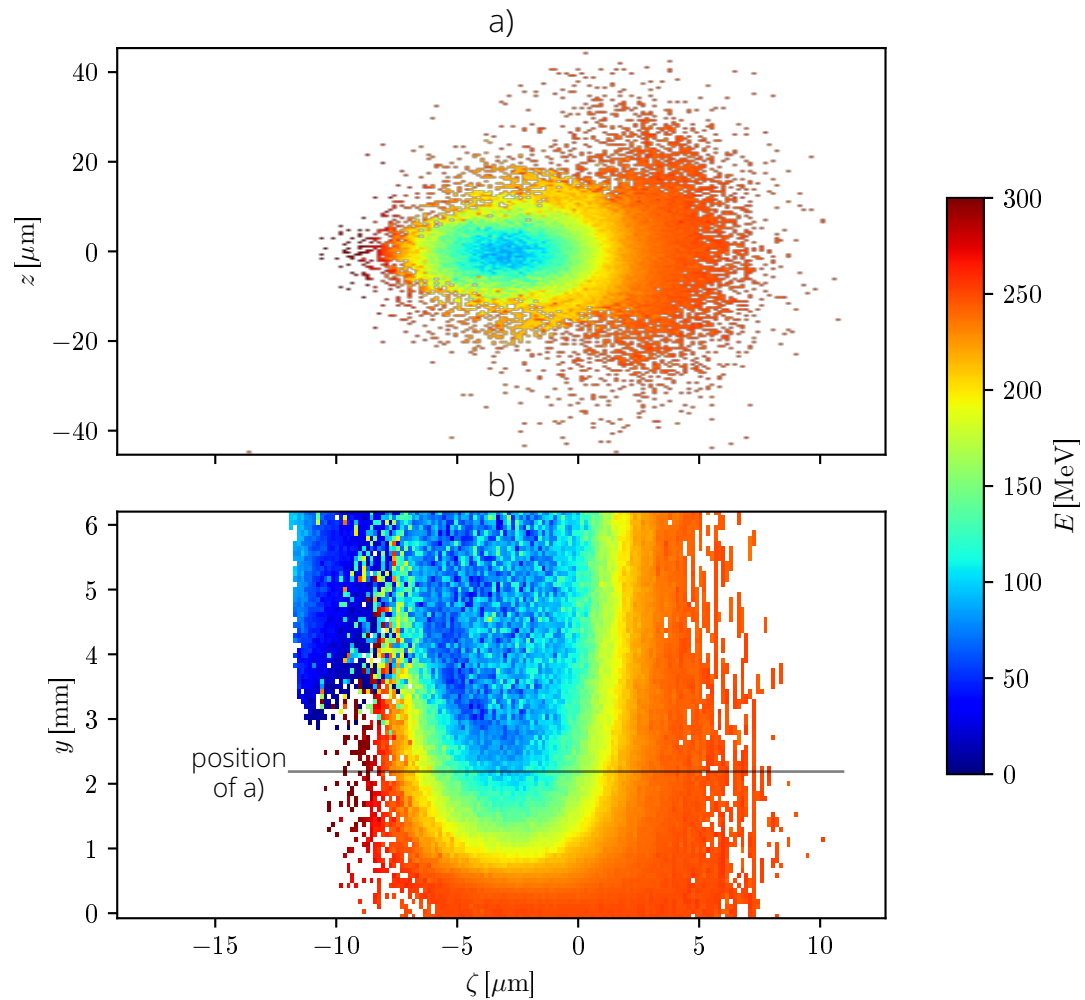
Figure 4.14.: Mean energy of the particles in the spatial bins. **(a)** ($y = 2.19\,\text{mm}$) Energy map over ζ-z- The bins measure $0.16\,\mu\text{m} \times 0.45\,\mu\text{m}$. Every bin with at least one particle is plotted (So no information about the energy density can be derived). Most energy is lost by particles in the center of the bunch at the peak decelerating field. **(b)** Mean energy of the particles in the bins over time. Only the bins around $z = 0$ are plotted and averaged in x-direction for every timestep, showing the gradually loss of energy in the middle of the driver until bunch breakup.
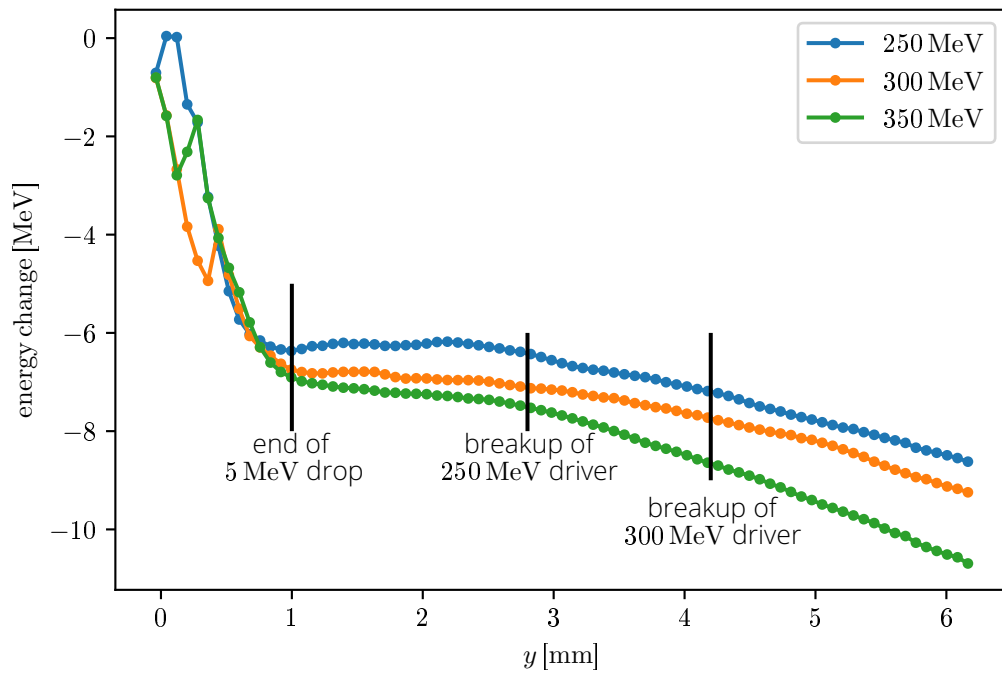
Figure 4.15.: Loss of peak energy for different initial energies are plotted over distance in plasma y.
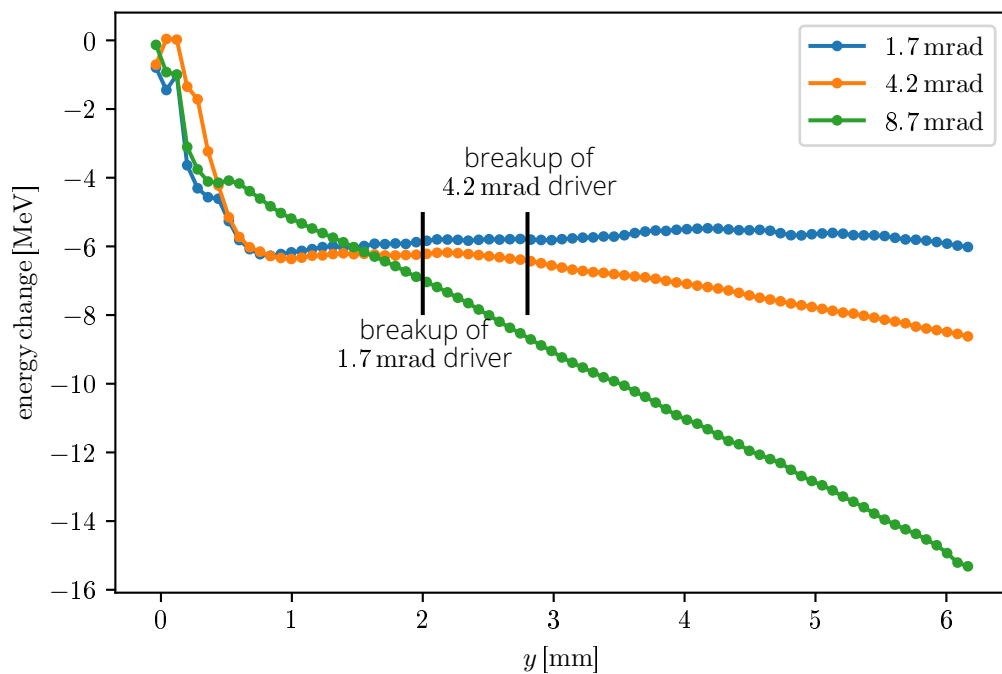

Figure 4.16.: Loss of peak energy for different initial divergences are plotted over y.

5. Conclusion and Outlook

The transformation of the shape of a PWFA driver was studied. Similar stages, like the formation of a tail and the spreading of wings, could be observed independent of initial conditions. Only the time needed for each stage and the occurrence of bunch breakup seem to depend on the initial conditions.

Analysis on the possible energy gain of a potential witness beam for different initial parameters suggests that the reduction of divergence has a more substantial effect on the maximal energy gain than an increased kinetic energy of the driver. The plus in energy gain decreases when increasing the beam energy. Efforts to achieve higher driver energies would result in a diminishing return of witness energy gain, making it possibly unprofitable. Meanwhile, new effects come into play when reducing the beam divergence, with a considerable part of the bunch breaking up and creating smaller cavities in a blowout regime. This results in a doubling of the maximal energy gain. The change in driver current was suggested as the cause of the differences between different divergences. This needs to be confirmed by future simulations.

Decreasing the divergence far below the used 4.3 mrad is hard to achieve in experiment. The divergence threshold for the premature bunch breakup should therefore be investigated in future studies as well, as it can result in strong increases of witness bunch energy. Other questions arise about the exact scaling of driver energy to maximal gained witness energy and if it is reasonable to invest in high-energy beams. Similar to the low divergence drivers, additional effects could come into play for higher energies of the driver. This would encourage further increases beyond the energies used currently in experiments and in this study. Additional research on the impact of the distance between the LWFA stage, the metal foil and the PWFA stage is also needed in the future, as this distance should have additional effects on the driver current.

Also presented was a study on the changes of the peak energy for different initial parameters. Energy losses ranging from 8 MeV to 11 MeV were observed, with an initial fast energy loss of 6 MeV for all drivers. These small energy changes are hard to detect in experiments, but they will become relevant when higher accuracy in the energy-charge correlation of the beam loaded LWFA bunch is achieved. Additionally, a correlation between the initial kinetic energy of the driver and total loss of peak energy was shown. Thus, a high-energy beam and a long enough gas jet help to produce energy losses that are significant in experiment. A correlation between the breakup of the bunch and peak energy loss could not be shown.

In any case, caution is needed in the future when using the peak energy as a measurement tool. The results suggest that for 3 mm long plasma jets with the tested parameters, a constant value of 5 MeV to 7 MeV needs to be added for correction, resulting in charge correction of

10 pC to 15 pC. For present-day experiments with uncertainties of 80 pC [7] on the charge reconstruction, this may not be significant but should be considered in the future when the uncertainty gets reduced. Future research on the energy loss for different parameters of the driver and plasma should be conducted. Better data fits of the energy peaks would reduce possible statistical artifacts and give higher certainty on the slow energy loss after the initial drop-off.

A. Approximation for spatial derivative

The full calculation of the numerical spacial derivatives through central finite differences up to the eighth order for the last two Maxwell equations can be found below. It is based on Equation 2.7 and Equation 2.8, taken from reference [11]. Only one of the three components for each field is shown here.

$$
\begin{aligned}
\frac{B_x|_{i,j+1/2,k+1/2}^{n+3/2} - B_x|_{i,j+1/2,k+1/2}^{n+1/2}}{\Delta t} = {} & 1.196 \left(\frac{E_y|_{i,j+1/2,k+1}^{n+1} - E_y|_{i,j+1/2,k}^{n+1}}{\Delta z} - \frac{E_z|_{i,j+1,k+1/2}^{n+1} - E_z|_{i,j,k+1/2}^{n+1}}{\Delta y} \right) \\
& -7.975 \cdot 10^{-2} \left(\frac{E_y|_{i,j+1/2,k+2}^{n+1} - E_y|_{i,j+1/2,k-1}^{n+1}}{\Delta z} - \frac{E_z|_{i,j+2,k+1/2}^{n+1} - E_z|_{i,j-1,k+1/2}^{n+1}}{\Delta y} \right) \\
& +9.570 \cdot 10^{-3} \left(\frac{E_y|_{i,j+1/2,k+3}^{n+1} - E_y|_{i,j+1/2,k-2}^{n+1}}{\Delta z} - \frac{E_z|_{i,j+3,k+1/2}^{n+1} - E_z|_{i,j-2,k+1/2}^{n+1}}{\Delta y} \right) \\
& -6.975 \cdot 10^{-4} \left(\frac{E_y|_{i,j+1/2,k+4}^{n+1} - E_y|_{i,j+1/2,k-3}^{n+1}}{\Delta z} - \frac{E_z|_{i,j+4,k+1/2}^{n+1} - E_z|_{i,j-3,k+1/2}^{n+1}}{\Delta y} \right)
\end{aligned}
$$

$$
\begin{aligned}
\frac{E_y|_{i,j+1/2,k}^{n+1} - E_y|_{i,j+1/2,k}^{n}}{c^2 \Delta t} = {} & 1.196 \left(\frac{B_x|_{i,j+1/2,k+1/2}^{n+1/2} - B_x|_{i,j+1/2,k-1/2}^{n+1/2}}{\Delta z} - \frac{B_z|_{i+1/2,j+1/2,k}^{n+1/2} - B_z|_{i-1/2,j+1/2,k}^{n+1/2}}{\Delta x} \right) \\
& -7.975 \cdot 10^{-2} \left(\frac{B_x|_{i,j+1/2,k+3/2}^{n+1/2} - B_x|_{i,j+1/2,k-3/2}^{n+1/2}}{\Delta z} - \frac{B_z|_{i+3/2,j+1/2,k}^{n+1/2} - B_z|_{i-3/2,j+1/2,k}^{n+1/2}}{\Delta x} \right) \\
& +9.570 \cdot 10^{-3} \left(\frac{B_x|_{i,j+1/2,k+5/2}^{n+1/2} - B_x|_{i,j+1/2,k-5/2}^{n+1/2}}{\Delta z} - \frac{B_z|_{i+5/2,j+1/2,k}^{n+1/2} - B_z|_{i-5/2,j+1/2,k}^{n+1/2}}{\Delta x} \right) \\
& -6.975 \cdot 10^{-4} \left(\frac{B_x|_{i,j+1/2,k+7/2}^{n+1/2} - B_x|_{i,j+1/2,k-7/2}^{n+1/2}}{\Delta z} - \frac{B_z|_{i+7/2,j+1/2,k}^{n+1/2} - B_z|_{i-7/2,j+1/2,k}^{n+1/2}}{\Delta x} \right) \\
& -\mu_0 J_y|_{i,j+1/2,k}^{n+1/2}
\end{aligned}
$$

Bibliography

[1] V Malka. "Plasma Wake Accelerators: Introduction and Historical Overview". en. In: *CERN Yellow Reports* (2016), Vol 1 (2016): Proceedings of the 2014 CAS–CERN Accelerator School: Plasma Wake Acceleration. DOI: `10.5170/CERN-2016-001.1` (cit. on p. 1).

[2] G Aad et al. "Observation of a new particle in the search for the Standard Model Higgs boson with the ATLAS detector at the LHC". In: *Physics Letters B* 716.1 (2012), pp. 1–29. DOI: `10.1016/j.physletb.2012.08.020` (cit. on p. 1).

[3] T Tajima and JM Dawson. "Laser Electron Accelerator". In: *Physical Review Letters* 43.4 (1979), pp. 267–270. DOI: `10.1103/physrevlett.43.267` (cit. on p. 1).

[4] P Chen, JM Dawson, RW Huff, and T Katsouleas. "Acceleration of Electrons by the Interaction of a Bunched Electron Beam with a Plasma". In: *Physical Review Letters* 54.7 (1985), pp. 693–696. DOI: `10.1103/physrevlett.54.693` (cit. on pp. 1, 3).

[5] AM de la Ossa et al. "Hybrid LWFA–PWFA staging as a beam energy and brightness transformer: conceptual design and simulations". In: *Philosophical Transactions of the Royal Society A: Mathematical, Physical and Engineering Sciences* 377.2151 (2019), p. 20180175. DOI: `10.1098/rsta.2018.0175` (cit. on pp. 1, 5).

[6] T Kurz et al. "Demonstration of a compact plasma accelerator powered by laser-accelerated electron beams". In: *Nature Communications* 12.1 (2021). DOI: `10.1038/s41467-021-23000-7` (cit. on pp. 1, 4, 11, 14).

[7] S Schöbel et al. "Effect of driver charge on wakefield characteristics in a plasma accelerator probed by femtosecond shadowgraphy". In: *New Journal of Physics* 24.8 (2022), p. 083034. DOI: `10.1088/1367-2630/ac87c9` (cit. on pp. 2–4, 11, 14, 17, 23, 29, 32, 36).

[8] S Gessner et al. "Demonstration of a positron beam-driven hollow channel plasma wakefield accelerator". In: *Nature Communications* 7.1 (2016). DOI: `10.1038/ncomms11785` (cit. on p. 3).

[9] T Kurz. "Realization of a compact plasma accelelerator for high quality electron beams". PhD thesis. TU Dresden / HZDR, 2020 (cit. on p. 4).

[10] M Bussmann et al. "Radiative Signatures of the Relativistic Kelvin-Helmholtz Instability". In: *Proceedings of the International Conference on High Performance Computing, Networking, Storage and Analysis*. SC '13. Denver, Colorado: ACM, 2013, 5:1–5:12. ISBN: 978-1-4503-2378-9. DOI: `10.1145/2503210.2504564` (cit. on p. 5).

[11] M Bussmann, S Bastrakov, A Debus, M Garten, A Huebl, P Ordyna, R Pausch, F Poeschel, K Steiniger, and R Widera. *PIConGPU: Performance-Portable Particle-in-Cell Simulations for the Exascale Era*. 2022. URL: `https://github.com/ComputationalRadiationPhysics/picongpu` (cit. on pp. 5, 7–9, 37).

[12] J Derouillat. *SMILEI: A collaborative, open-source, multi-purpose particle-in-cell code for plasma simulation*. 2017. DOI: `10.17632/GSN4X6MBRG.1`. URL: `https://github.com/SmileiPIC/Smilei` (cit. on p. 5).

[13] AA Vlasov. "THE VIBRATIONAL PROPERTIES OF AN ELECTRON GAS". In: *Soviet Physics Uspekhi* 10.6 (1968), pp. 721–733. DOI: `10.1070/pu1968v010n06abeh003709` (cit. on p. 5).

[14] A Huebl. "PIConGPU: Predictive Simulations of Laser-Particle Accelerators with Manycore Hardware". en. PhD thesis. TU Dresden and HZDR, 2019. DOI: `10.5281/ZENODO.3266820` (cit. on pp. 6, 7).

[15] R Pausch. "Synthetic radiation diagnostics as apathway for studying plasmadynamics from advanced accelerators to astrophysical observations". PhD thesis. TU Dresden / HZDR, 2019. URL: `https://www.hzdr.de/publications/Publ-29259` (cit. on pp. 6, 8).

[16] H Burau, R Widera, W Hönig, G Juckeland, A Debus, T Kluge, U Schramm, TE Cowan, R Sauerbrey, and M Bussmann. "PIConGPU: A Fully Relativistic Particle-in-Cell Code for a GPU Cluster". In: *IEEE Transactions on Plasma Science* 38.10 (2010), pp. 2831–2839. DOI: `10.1109/tps.2010.2064310` (cit. on p. 6).

[17] K Yee. "Numerical solution of initial boundary value problems involving maxwell's equations in isotropic media". In: *IEEE Transactions on Antennas and Propagation* 14.3 (1966), pp. 302–307. DOI: `10.1109/tap.1966.1138693` (cit. on p. 7).

[18] JP Boris. "Relativistic Plasma Simulation - Optimization of a Hybrid Code". In: *Proceedings of 4th Conference on Numerical Simulation of Plasmas* (1970), pp. 3–67 (cit. on p. 7).

[19] S Zenitani and T Umeda. "On the Boris solver in particle-in-cell simulation". In: *Physics of Plasmas* 25.11 (2018), p. 112110. DOI: `10.1063/1.5051077` (cit. on p. 8).

[20] TZ Esirkepov. "Exact charge conservation scheme for Particle-in-Cell simulation with an arbitrary form-factor". In: *Computer Physics Communications* 135.2 (2001), pp. 144–153. DOI: `10.1016/s0010-4655(00)00228-9` (cit. on p. 8).

[21] R Lehe, A Lifschitz, C Thaury, V Malka, and X Davoine. "Numerical growth of emittance in simulations of laser-wakefield acceleration". In: *Physical Review Special Topics - Accelerators and Beams* 16.2 (2013), p. 021301. DOI: `10.1103/physrevstab.16.021301` (cit. on p. 9).

[22] A Huebl. "Injection Control for Electrons in Laser-Driven Plasma Wakes on the Femtosecond Time Scale". en. In: (2014). DOI: `10.5281/ZENODO.15924` (cit. on p. 10).

[23] A Huebl, F Poeschel, F Koller, and J Gu. *openPMD-api: C++ & Python API for Scientific I/O with openPMD*. Version 0.15.0-dev. 2018. DOI: `10.14278/rodare.27`. URL: `https://github.com/openPMD/openPMD-api` (cit. on p. 10).

[24] A Huebl, R Lehe, JL Vay, DP Grote, I Sbalzarini, S Kuschel, D Sagan, F Pérez, F Koller, and M Bussmann. *Openpmd 1.1.0: Base Paths For Mesh- And Particle-Only Files And Updated Attributes*. en. 2018. DOI: `10.5281/ZENODO.1167843` (cit. on p. 10).

[25] JPC Cabadağ et al. "Gas-dynamic density downramp injection in a beam-driven plasma wakefield accelerator". In: *Physical Review Research* 3.4 (2021), p. l042005. DOI: `10.1103/physrevresearch.3.l042005` (cit. on p. 11).

[26] G Raj et al. "Probing ultrafast magnetic-field generation by current filamentation instability in femtosecond relativistic laser-matter interactions". In: *Physical Review Research* 2.2 (2020), p. 023123. DOI: 10.1103/physrevresearch.2.023123 (cit. on p. 14).

[27] M Kirchen, S Jalas, P Messner, P Winkler, T Eichner, L Hübner, T Hülsenbusch, L Jeppe, T Parikh, M Schnepp, and AR Maier. "Optimal Beam Loading in a Laser-Plasma Accelerator". In: *Physical Review Letters* 126.17 (2021), p. 174801. DOI: 10.1103/physrevlett.126.174801 (cit. on p. 25).

[28] J Götzfried, A Döpp, M Gilljohann, F Foerster, H Ding, S Schindler, G Schilling, A Buck, L Veisz, and S Karsch. "Physics of High-Charge Electron Beams in Laser-Plasma Wakefields". In: *Physical Review X* 10.4 (2020), p. 041015. DOI: 10.1103/physrevx.10.041015 (cit. on p. 25).